

¹ A bistable autoregulatory module in ² the developing embryo commits ³ cells to binary fates

⁴ **Jiaxi Zhao^{1†}, Mindy Liu Perkins^{2†}, Matthew Norstad³, Hernan G. Garcia^{1,3,4,5,6*}**

*For correspondence:

hggarcia@berkeley.edu (HGG)

[†]These authors contributed equally to this work

⁵ ¹Department of Physics, University of California at Berkeley, Berkeley, CA 94720, USA;
⁶ ²Developmental Biology Unit, European Molecular Biology Laboratory, Heidelberg,
⁷ Germany; ³Department of Molecular and Cell Biology, University of California Berkeley,
⁸ Berkeley, CA 94720, USA; ⁴Biophysics Graduate Group, University of California at
⁹ Berkeley, Berkeley, CA 94720, USA; ⁵Institute for Quantitative Biosciences-QB3,
¹⁰ University of California at Berkeley, Berkeley, CA 94720, USA; ⁶Chan Zuckerberg Biohub,
¹¹ San Francisco, CA 94158, USA

¹²

¹³ **Abstract** Positive autoregulation has been repeatedly proposed as a mechanism for cells to
¹⁴ adopt binary fates during embryonic development through bistability. However, without
¹⁵ quantitatively determining their parameters, it is unclear whether the plethora of positive
¹⁶ autoregulatory modules found within developmental gene regulatory networks are actually
¹⁷ bistable. Here, we combine *in vivo* live imaging with mathematical modeling to dissect the binary
¹⁸ cell fate dynamics of the fruit fly pair-rule gene *fushi tarazu* (*ftz*), which is regulated by two known
¹⁹ enhancers: the early (non-autoregulating) element and the autoregulatory element. Live imaging
²⁰ of transcription and protein concentration in the blastoderm revealed that binary *Ftz* cell states
²¹ are achieved as *ftz* expression rapidly transitions from being dictated by the early element to the
²² autoregulatory element. Moreover, we discovered that *Ftz* concentration alone is insufficient to
²³ activate the autoregulatory element, and that this element only becomes responsive to *Ftz* at a
²⁴ prescribed developmental time. Based on these observations, we developed a dynamical
²⁵ systems model, and quantitated its kinetic parameters directly from experimental
²⁶ measurements. Our model demonstrated that the *ftz* autoregulatory module is indeed bistable
²⁷ and that the early element transiently establishes the content of the binary cell fate decision to
²⁸ which the autoregulatory module then commits. Further analysis *in silico* revealed that the
²⁹ autoregulatory element locks the *Ftz* expression fate quickly, within 35 min of exposure to the
³⁰ transient signal of the early element. Overall, our work confirms the widely held hypothesis that
³¹ autoregulation can establish developmental fates through bistability and, most importantly,
³² provides a framework for the quantitative dissection of cellular decision-making based on
³³ systems dynamics models and real-time measurements of transcriptional and protein dynamics.

³⁴

35 1 Introduction

36 One of the central questions in developmental biology concerns how cells precisely and irreversibly
37 adopt distinct cellular fates. It has been argued that cells assume their unique gene expression pro-
38 files through a sequence of decisions among branching paths ([Zernicka-Goetz et al., 2009; Soldatov](#)
39 [et al., 2019](#)), most famously encapsulated by C. H. Waddington's "epigenetic landscape" of peaks
40 and valleys delineating the possible trajectories that a cell can follow ([Waddington, 1957](#)). Genetic
41 networks that lock a cell into one of these trajectories may be thought of as "memory modules" that
42 guide cells through valleys in the landscape to their ultimate fates. In the simplest case, where a
43 decision is made between two alternative developmental fates, the memory module is binary and
44 is often referred to as a switch. The state of the switch is set by the action of transient upstream
45 regulatory signals.

46 Several genetic motifs, such as autoactivation and mutual repression, have been identified that
47 are capable of maintaining binary cell fates ([Alon, 2007; Peter and Davidson, 2015](#)). However, the
48 mere presence of a motif is insufficient to guarantee that a network can remember its expression
49 state once upstream regulators have degraded. The ability to lock onto high or low expression
50 levels results from bistability ([Box 1](#)), a systems-level property that depends upon the quantitative
51 details of the kinetics of the involved chemical reactions ([Ferrell, 2002; Angeli et al., 2004; Graham](#)
52 [et al., 2010](#)).

53 Despite the widespread invocation of bistability to explain the stable and irreversible determi-
54 nation of cellular fates ([Peter and Davidson, 2015](#)), relatively little quantitative data exist to confirm
55 bistability in gene expression modules within developing embryos. Previous studies in cell culture
56 and fixed embryos have provided evidence for the existence of bistability in hematopoietic differ-
57 entiation ([Laslo et al., 2006; Kueh et al., 2013](#)), the Shh network ([Lai et al., 2004](#)), the vertebrate
58 hindbrain ([Bouchoucha et al., 2013](#)), between the BMP and FGF morphogens ([Srinivasan et al.,](#)
59 [2014](#)), and within the Notch-Delta signaling system ([Sprinzak et al., 2010](#)). Quantitative evidence
60 for multistability in fruit fly embryos has also been derived from fitting the parameters of high-
61 dimensional network models to measurements in fixed tissue ([von Dassow et al., 2000; Jaeger](#)
62 [et al., 2004; Lopes et al., 2008; Manu et al., 2009; Papatsenko and Levine, 2011; Verd et al., 2017](#)).

63 While these models are capable of reproducing the observed phenomenology, there is often no
64 guarantee that the optimal set of inferred parameter values reflects actual biophysical quantities
65 ([Gutenkunst et al., 2007; Cotterell and Sharpe, 2010; Villaverde et al., 2015; Wieland et al., 2021](#)).

66 Thus, it is important to verify that the conclusions drawn from computational modeling and *in vitro*
67 experiments apply to developmental systems *in vivo* in the context of models that quantitatively
68 capture the molecular interactions that underlie the process of cellular decision making. To the
69 best of our knowledge, evidence for the bistability of a genetic module based on these molecular
70 interactions in an intact multicellular organism has not yet been demonstrated.

71 The early development of the fruit fly *Drosophila melanogaster* is an ideal model system for
72 studying binary cell fate decision making. Specifically, the mapping of the regulation of *fushi tarazu*
73 (*ftz*), one of the *Drosophila* pair-rule genes that forms seven discrete stripes at the cellular blasto-
74 derm stage prior to gastrulation (2.5 - 3.5 hours after fertilization; [Nüsslein-Volhard and Wieschaus](#)
75 ([1980](#)); [Hafen et al. \(1984\)](#); [Wakimoto et al. \(1984\)](#); [Weiner et al. \(1984\)](#); [Hiromi et al. \(1985\)](#)), has
76 suggested that this gene is capable of autoactivation ([Hiromi and Gehring, 1987](#)). These studies
77 showed that two main enhancers—the early, or zebra, element and the autoregulatory element—
78 dictate *Ftz* protein expression during early embryogenesis ([Figure 1A; Hiromi and Gehring \(1987\)](#)).
79 The early element responds to upstream transcription factors such as the gap genes to establish
80 the initial expression pattern of seven stripes ([Dearolf et al., 1989](#)). This element is functionally dis-
81 tinct from the autoregulatory element, which contains multiple *Ftz* binding sites that allow *Ftz* to
82 activate its own expression ([Pick et al., 1990; Schier and Gehring, 1992, 1993](#)). This autoactivation

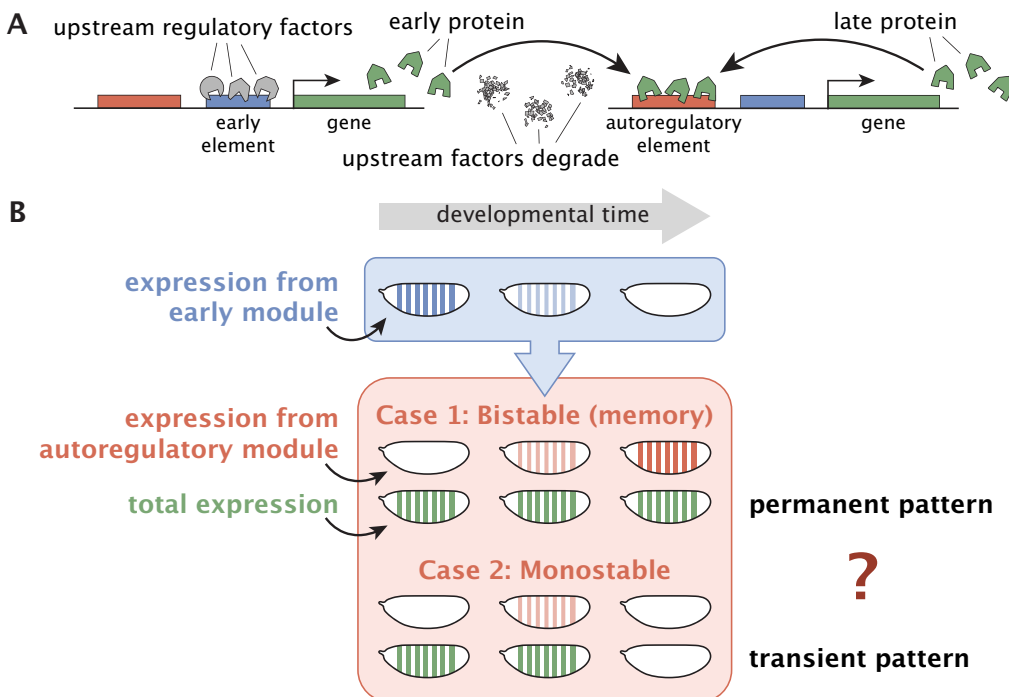


Figure 1. The bistability of the autoregulatory module can determine cell fate. (A) The autoregulatory architecture consists of an early element to which upstream factors bind to transiently upregulate gene expression of an activator, and an autoregulatory element to which the activator binds to, under certain circumstances, promote its own expression even once the upstream factors have degraded. (B) The total activator concentration (green) is a sum of the protein produced by the early (blue) and autoregulatory (red) modules. If the autoregulatory module is bistable, it possesses binary memory that permits transiently high concentrations of early protein to be locked into permanent high expression levels (high cell fate). If, in contrast, the autoregulatory module is monostable, then it may transiently boost protein levels from the early module, but over time all cells will ultimately revert to the same low fate.

network motif is theoretically capable of exhibiting bistability and has therefore been hypothesized to act as a binary memory module ([Alon, 2007; Xiong and Ferrell, 2007](#)).

Whether a cell possesses a memory module determines whether observed states of gene expression are transient in the absence of continued external signaling, or whether these states can be locked into permanent cell fates that can be maintained without further intervention. Specifically, if the autoregulatory module is bistable, then high *ftz* expression driven by the transient presence of upstream factors is stabilized by the autoregulatory element into a permanent cell fate ([Figure 1B](#), case 1), even once those factors degrade (or until further regulatory mechanisms intervene). If, instead, the autoregulatory element is monostable, then the observed separation of *Ftz* concentration into high and low levels persists only as long as upstream factors are present to regulate expression. In their absence, *Ftz* expression would revert to a single fate for all cells ([Figure 1B](#), case 2). It is important to note, however, that in this case, the transiently high or low trajectory of *Ftz* concentration could still be instructive for regulating downstream genes.

Here, we characterize the *ftz* autoregulatory module *in vivo* through quantitative real-time measurements in living fruit fly embryos. We focus on the anterior boundary of stripe 4, the only *Ftz* stripe that has been shown to be driven exclusively by the early and autoregulatory elements and not by other enhancers in the gene's vicinity ([Schroeder et al., 2011; Graham et al., 2021](#)). We observe that *Ftz* expression separates into high and low levels at the blastoderm stage during the

101 20 min prior to gastrulation, concurrent with a transition in regulatory control from the early to
102 the autoregulatory element. We discover that autoregulation is triggered at a specific time point in
103 development—presumably through the action of “timer genes” ([Clark and Akam, 2016; Clark and](#)
104 [Peel, 2018; Clark et al., 2022](#))—rather than through a readout of Ftz concentration alone. Based on
105 these observations, we develop a dynamical systems model and quantitate its parameters from
106 simultaneous real-time measurements of *ftz* transcription and Ftz protein dynamics in single cells
107 of living embryos. Our model predicts binary Ftz expression levels at gastrulation with high accu-
108 racy and demonstrates that, indeed, the *ftz* autoregulatory module is bistable. We conclude that
109 the *ftz* autoregulatory element acts as a memory module to commit cells to binary fates that are
110 otherwise transiently defined by the early element, thereby validating a long-standing hypothesis
111 in developmental and systems biology. Simulations further make it possible to quantitatively de-
112 fine a developmental commitment window, which shows that the autoregulatory module requires
113 about half an hour to establish a memory of the transient signal from the early module. Thus, our
114 work provides a framework for the dissection of other regulatory modules in the gene regulatory
115 networks that dictate development based on this interplay between dynamical systems models
116 and real-time experiments.

117 2 Results

118 2.1 Binary cell states of Ftz expression are established in early development

119 To understand the role of positive autoregulation in deciding Ftz expression levels, we first sought
120 to visualize and track Ftz protein dynamics over time. We used CRISPR-mediated recombination
121 ([Gratz et al., 2015](#)) to fuse a LlamaTag, a fluorescent probe that reports on the fast protein dynamics
122 that characterize early embryonic development, to the C-terminus of the endogenous Ftz protein
123 ([Figure 2A; Bothma et al. \(2018\)](#)). An examination of the fluorescently labeled Ftz protein in the
124 early embryo shows that, around 15 min before gastrulation, Ftz protein is expressed in a seven-
125 stripe pattern with clear, smooth boundaries ([Figure 2B, left](#)). This expression pattern refines over
126 the following 15 min into sharp stripe boundaries by the start of gastrulation ([Figure 2B, right](#)). The
127 result shows that cells express either high or low levels of Ftz protein, as pictured in [Figure 2C](#) for
128 the anterior boundary of stripe 4, consistent with results from previous studies ([Schroeder et al.,](#)
129 [2011; Clark, 2017; Bothma et al., 2018](#)).

130 Our live imaging measurements allowed us to quantitatively examine the dynamics with which
131 binary cell states are established by calculating the Ftz protein distribution in individual nuclei at
132 different time points in development ([Figure 2D](#)). Our analysis revealed that the expression level
133 is initially unimodal across all cells ([Figure 2D, top and E](#)) and then evolves into a bimodal distri-
134 bution within 15 min ([Figure 2D, bottom and E](#)). Consistent with our qualitative observations in
135 [Figure 2B and C](#), cells at these later times can be quantitatively classified into distinct “high-Ftz”
136 and “low-Ftz” cell states using a single threshold ([Figure 2D, bottom and E](#)), which indicates that
137 binary cell states are already established prior to the onset of gastrulation. Moreover, though the
138 two cell states are clearly distinguishable from each other, we observed that there is significant
139 cell-to-cell variability within both states. Specifically, the single-nucleus Ftz protein distribution for
140 high-Ftz levels spans more than a two-fold range ([Figure 2D, bottom and E](#)).

141 Previous studies have established that autoregulation plays a key role during *ftz* expression: a
142 lack of the *ftz* autoregulatory element or mutated Ftz binding sites within the element result in the
143 loss of Ftz expression at later developmental stages ([Hiromi and Gehring, 1987; Schier and Gehring,](#)
144 [1992](#)). However, it is unclear at what developmental time *ftz* autoregulation is initiated in response
145 to the Ftz expression stemming from the early element. Specifically, is the autoregulatory element
146 active before stripes of Ftz expression emerge, or is autoregulation invoked after the early element
147 has already established this pattern? To distinguish between these two scenarios, we decoupled

Box 1. Bistability

A simplified dynamical systems model of the *ftz* autoregulatory element that ignores the dynamics of mRNA production describes the rate of change in *Ftz* concentration over time as

$$\frac{dP(t)}{dt} = f(P(t)) - \gamma P(t) \quad (1)$$

where P is *Ftz* concentration, $f(P)$ is the gene regulatory (or input-output) function that describes how input *Ftz* concentration controls the rate of *Ftz* production, and γ is the *Ftz* degradation rate. Since *Ftz* promotes its own production, $f(P)$ increases with P .

In the long term, *Ftz* concentrations will tend toward stable *steady states*, or attractors, for which (by definition) the change in concentration over time goes to 0 (i.e., $\frac{dP}{dt} = 0$). Attractors are stable, meaning that if *Ftz* concentration is perturbed slightly away from the attractor, it will eventually return to the attractor. However, it is also possible to have unstable steady states for which, after a small perturbation, *Ftz* concentration will evolve away from the steady state. For the system in **Eq. 1**, a steady state P^* will solve

$$\gamma P^* = f(P^*), \quad (2)$$

meaning that all steady states can be found graphically as the intersections between a line of slope γ and the function f . In our case, the gene regulatory function f is a sigmoidal function (red curves in Figure B1), such that there are between 1 and 3 intersections of the total degradation rate γP with the *Ftz* production rate $f(P)$. Then the autoregulatory module is either monostable, meaning it possesses one attractor, or bistable, meaning it possesses two attractors and one unstable steady state between these attractors. Since the number of intersections depends on the shape of f and the slope γ , the exact parameter values are crucial for determining the possible behaviors that can be exhibited by the autoregulatory module.

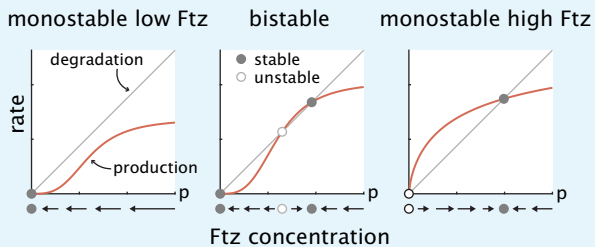


Figure B1. Above, steady states are identified through the intersection of the production rate $f(P)$ with the total degradation rate γP where p is the *Ftz* concentration. Below, vector fields show the direction *Ftz* concentration will evolve over time. An equivalent graphical test also exists for 2D dynamical systems models where mRNA is modeled explicitly; see **Section S1.3**.

We will also consider controlled systems, i.e., dynamical systems that have an additional regulatory input. In this case, this input corresponds to the *Ftz* concentration produced by the early element, P_{early} , such that the dynamics of *Ftz* production by the autoregulatory element are given by

$$\frac{dP_{late}(t)}{dt} = f(P_{late}(t) + P_{early}(t)) - \gamma P_{late}(t). \quad (3)$$

Since the early element shuts down over time (that is, $P_{early}(\infty) = 0$), the steady states P_{late} in **Eq. 3** are the same as those for P in **Eq. 1**. However, the transient dynamics of P_{early} shape the trajectory P_{late} will take and determine which steady state *Ftz* will ultimately reach.

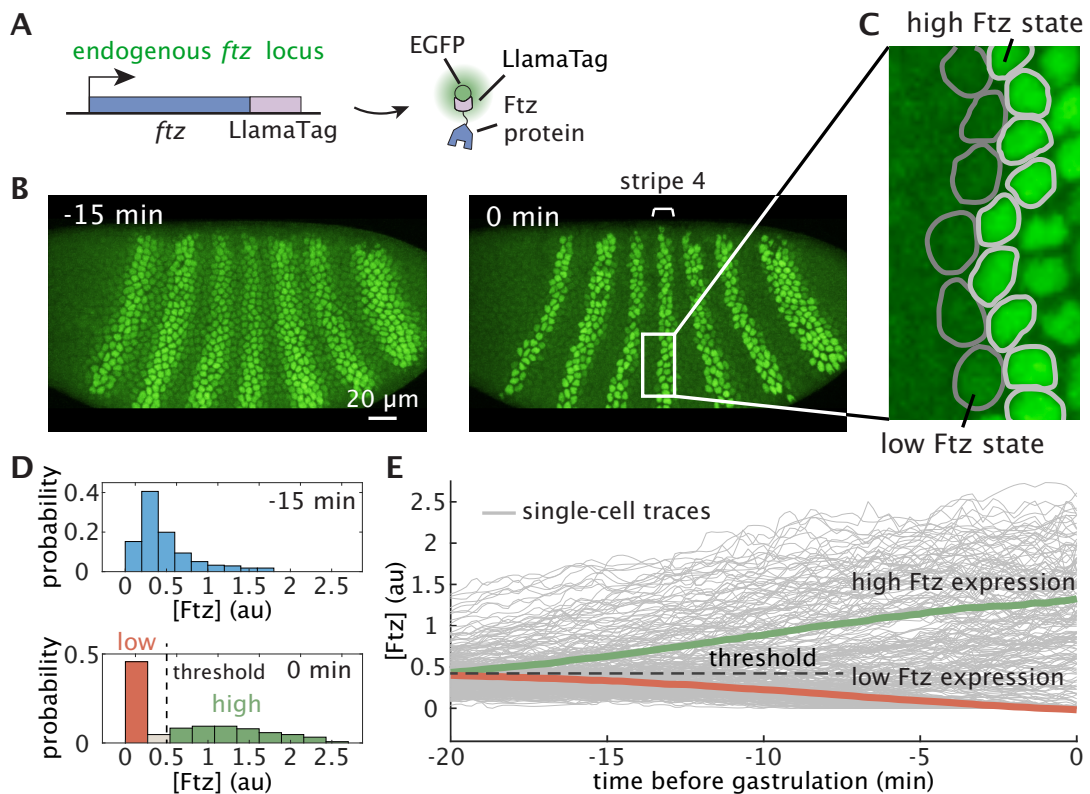


Figure 2. Binary cell states are rapidly established prior to gastrulation. (A) A fusion of endogenous Ftz to a LlamaTag makes it possible to visualize the highly dynamic Ftz protein pattern in the early fly embryo. Once Ftz protein is translated in the cytoplasm, LlamaTag binds to maternally deposited EGFP and is transported into the nucleus, increasing nuclear fluorescence to produce a direct readout of Ftz protein concentration. (B) Snapshots from a movie capturing Ftz protein concentration dynamics. The anterior side of the embryo is oriented towards the left, and the time is given relative to gastrulation. (C) Ftz expression along the anterior boundary of stripe 4 shows a discrete transition between distinct cell states. (D) Histograms of single-nucleus fluorescence values at different developmental time points show that a single threshold can be used to classify cells into “high-Ftz” and “low-Ftz” cell states prior to gastrulation. (E) Single-cell trajectories of nuclei at the anterior boundaries of Ftz stripe 4. Green and red lines are averages for nuclei determined to ultimately have “high-Ftz” and “low-Ftz” levels at gastrulation, respectively, as defined in (D).

148 the transcriptional dynamics driven by the early and autoregulatory elements by creating two sep-
149 arate reporter constructs, each containing only the early or autoregulatory elements followed by
150 MS2 stem-loops that enable the direct visualization of transcriptional dynamics ([Figure 3A; Garcia](#)
151 [et al. \(2013\); Lucas et al. \(2013\)](#)).

152 We observed that the early element already drives a relatively constant gene expression level
153 around 20 min prior to gastrulation ([Figure 3B and C](#)). Then, at 15 min before gastrulation, its trans-
154 scriptional activity decreases significantly, resulting in a 60% reduction within the next 20 min of
155 development ([Figure 3B and C](#)). Conversely, autoregulation is initiated 20 min prior to gastrulation,
156 with its activity increasing until gastrulation starts ([Figure 3C](#)). This transition between the early
157 and autoregulatory elements occurs while binary cell states are being established ([Figure 2](#)). Since
158 autoregulation becomes the dominant driver of Ftz expression after this transition, it is likely that
159 autoregulation plays a key role in Ftz-mediated decision-making prior to gastrulation.

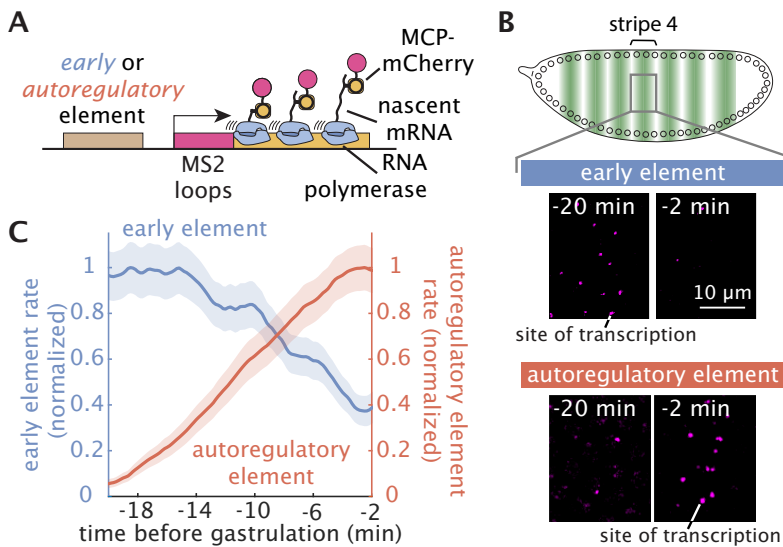


Figure 3. A sequential transition in *Ftz* regulation from the early to the autoregulatory element occurs during the establishment of discrete cell states. (A) Imaging transcriptional dynamics of the early and autoregulatory elements using the MS2 system. Maternally deposited MS2 coat protein (MCP) fused to mCherry binds to MS2 stem-loops in the nascent RNA of the reporter construct. (B) Snapshots of sites of nascent transcript formation labeled by MS2 from reporters of the early and autoregulatory elements at different time points reveal that transcription from the early element is reduced significantly as gastrulation approaches and that transcription driven by the autoregulatory element increases shortly before gastrulation. (C) Quantification of the transcriptional activity reported by the MS2 fluorescence from the early ($N = 3$ embryos) and autoregulatory ($N = 7$ embryos) elements as a function of time confirms that, within 20 min, *ftz* gene expression transitions from originating mainly from the early element to being dominated by the autoregulatory element. MS2 traces are smoothed using a moving average of 5 min. Error bars shown indicate standard errors over multiple embryos.

160 2.2 *ftz* autoactivation is triggered at a specific developmental time

161 The tight transition between the early and autoregulatory elements that occurs within 20 min (**Figure 3**) could be indicative of autoactivation being initiated by the increase in *Ftz* concentration
162 driven by the early element. However, autoactivation could also be triggered by upstream factors
163 at a specific developmental time, regardless of the *Ftz* level at that time point.

164 To distinguish between these two scenarios, we measured the gene regulatory function—the
165 input-output function describing how the input *Ftz* concentration dictates the output rate of *ftz*
166 transcription—of the *ftz* autoregulatory element at distinct developmental times. If autoactivation
167 is solely initiated by *Ftz* produced by the early element, the regulatory function should remain
168 constant throughout development. On the other hand, if autoregulation is triggered through an
169 independent mechanism—such as activation mediated by other transcription factors at a given
170 developmental time—then the *ftz* autoregulatory element should be unresponsive to input *Ftz*
171 protein before this developmental time point.

172 We measured the gene regulatory function of the autoregulatory element by constructing an
173 experimental system that allows for the simultaneous monitoring of *Ftz* concentration and the
174 corresponding autoregulatory activity. We used the tagged endogenous *Ftz* protein as the input
175 and introduced a transgenic reporter with MS2 loops under the control of the *ftz* autoregulatory
176 element as the output (**Figure 4A**). Live imaging of the anterior boundary of *Ftz* stripe 4 (**Figure 4B**)
177 showed that, initially, around 25 min prior to gastrulation, both *Ftz* expression and the autoregu-
178 latory response were relatively low, and later increased as development progressed. Just before
179 gastrulation, the *Ftz* protein pattern refined into a discrete boundary, with the *ftz* autoregulatory
180

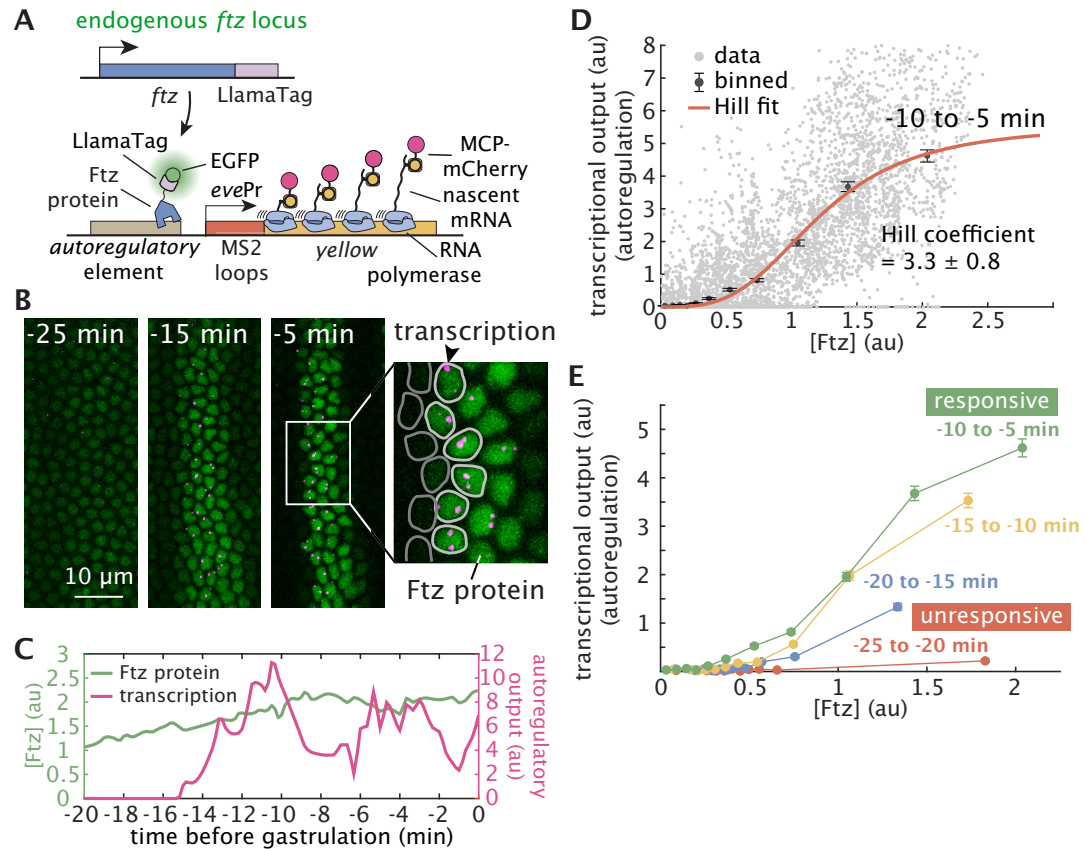


Figure 4. Two color live-imaging reveals that *ftz* autoregulation is initiated at a specific developmental time. (A) Two-color tagging permits *in vivo* simultaneous visualization of input Ftz protein concentration using a LlamaTag and output autoregulatory transcriptional dynamics using a reporter carrying the MS2 system. (B) Representative frames from live-imaging data. Green and magenta channels correspond to Ftz concentration and the transcriptional output from the *ftz* autoregulatory element, respectively. Dark gray and light gray outlines correspond to cells expressing high or low levels of Ftz protein, respectively. (C) Illustrative single-cell trace of Ftz protein and autoregulatory activity. Green and magenta lines correspond to the Ftz protein and transcriptional activity of the autoregulatory element, respectively. Both protein and MS2 traces are smoothed using a moving average of 1 min. (D) Experimentally measured gene regulatory function of the *ftz* autoregulatory element between -10 min to -5 min relative to gastrulation. Grey points correspond to simultaneous measurements of Ftz and MS2 fluorescence at individual time points from single-cell traces at the anterior boundary of stripe 4 ($N = 211$ nuclei, example traces shown in [Figure S1](#)). These points were grouped into quantiles, and a Hill function (red line) was fit to the quantile means. (E) The autoregulatory input-output function evolves over time, as the *ftz* autoregulatory element transitions from an unresponsive state to a responsive state within 15 min, indicating that *ftz* autoregulation is initiated through a developmental time-based mechanism. Error bars shown indicate standard errors. All data are from $N = 7$ embryos.

181 response clearly following the stripe boundary (**Figure 4B**).

182 To calculate the regulatory function, we restricted our analysis to the cells at the anterior bound-
183 ary of stripe 4 as a means to minimize the influence of other position-dependent transcription fac-
184 tors that might also contribute to *ftz* autoactivation (**Schier and Gehring, 1993**). We first extracted
185 two rows (high and low) of boundary cells. Then, we separated the input Ftz concentration and
186 output transcription from the autoregulatory element in the data corresponding to each individ-
187 ual cell (**Figure 4C; Figure S1**) into ten quantiles and fit a Hill function to the quantile averages to get
188 the gene regulatory function of *ftz* autoregulation within a defined temporal range (for example,
189 -10 min to -5 min for **Figure 4D**). Our analysis revealed a sharp regulatory relationship between Ftz
190 protein and autoregulatory response, with a Hill coefficient of 3.3 ± 0.8 (**Figure 4D**). Such Hill coeffi-
191 cients are comparable to those estimated in the context of autoactivation in vertebrate hindbrain
192 development (**Bouchoucha et al., 2013**) as well as those observed in simpler regulatory motifs that
193 do not feature feedback (**Gregor et al., 2007**).

194 We repeated the process described above at multiple developmental times to analyze how
195 the regulatory function for *ftz* autoactivation evolves over time. The results, shown in **Figure 4E**,
196 revealed that the regulatory function is clearly distinct at different time points. Specifically, initially
197 around -25 min to -20 min, the *ftz* autoregulatory element is effectively unresponsive to input Ftz
198 protein (**Figure 4E**, red line). However, the element progressively transitions to a fully responsive
199 state within 15 min (**Figure 4E**, green line). The observed temporal evolution of the autoregulatory
200 element's responsiveness to Ftz protein is a clear indication that the autoregulatory element is not
201 always primed to respond to input Ftz protein and that, instead, its expression is triggered at a
202 specific developmental time, presumably by upstream transcription factors.

203 2.3 Mathematical modeling quantitatively predicts Ftz concentrations

204 As we argued in **Figure 1B**, the fact that Ftz can exhibit a high state at one point in time does not
205 necessarily imply that this high state will persist in the absence of upstream regulation. Determining
206 whether the autoregulatory module is bistable and hence possesses developmental memory
207 requires turning the schematic shown in **Figure 1A** into an explicit mathematical model with empir-
208 ically determined parameter values. To that end, we first developed a dynamical systems model
209 for the full Ftz regulatory system (including both the early and autoregulatory elements) to verify
210 whether we could accurately recapitulate experimental results *in silico*.

211 Our measurements revealed that the autoregulatory element is unresponsive to Ftz concentra-
212 tion until about $t_{on} = -20$ min (**Figure 4E**). Once the element becomes responsive, we can describe
213 the *ftz* autoregulatory module using the dynamical systems model given by

$$\begin{cases} \frac{dR_{late}}{dt} = cf(P_{early}(t) + P_{late}(t)) - \gamma_R R_{late}(t) \\ \frac{dP_{late}}{dt} = \alpha R_{late}(t) - \gamma_P P_{late}(t) \end{cases}, t \geq t_{on}, \quad (4)$$

214 where $R_{late}(t)$ and $P_{late}(t)$ are the mRNA and protein concentrations produced by the autoregulatory
215 module, γ_R, γ_P are the decay rates of mRNA and protein, respectively, and α is the translation rate.
216 $f(P)$ is the gene regulatory function measured for the transgene and shown in **Figure 4D** that de-
217 scribes the output rate of mRNA production as a function of the input Ftz concentration. Since both
218 the early and autoregulatory elements drive Ftz expression, the gene regulatory function depends
219 on $P_{total}(t)$ which is the sum of the protein contributions from the early ($P_{early}(t)$) and autoregula-
220 tory ($P_{late}(t)$) modules. c is a scaling factor between the transcriptional output of the endogenous
221 locus and the gene regulatory function, which was measured for a transgene (**Figure 4D**). The first
222 equation in the system shown in Eq. 4 then describes the dynamics of mRNA produced from the au-
223 toregulatory element as a result of its transcriptional activity (first term on the right-hand side) and
224 mRNA degradation (second term on the right-hand side). Further, the second equation describes

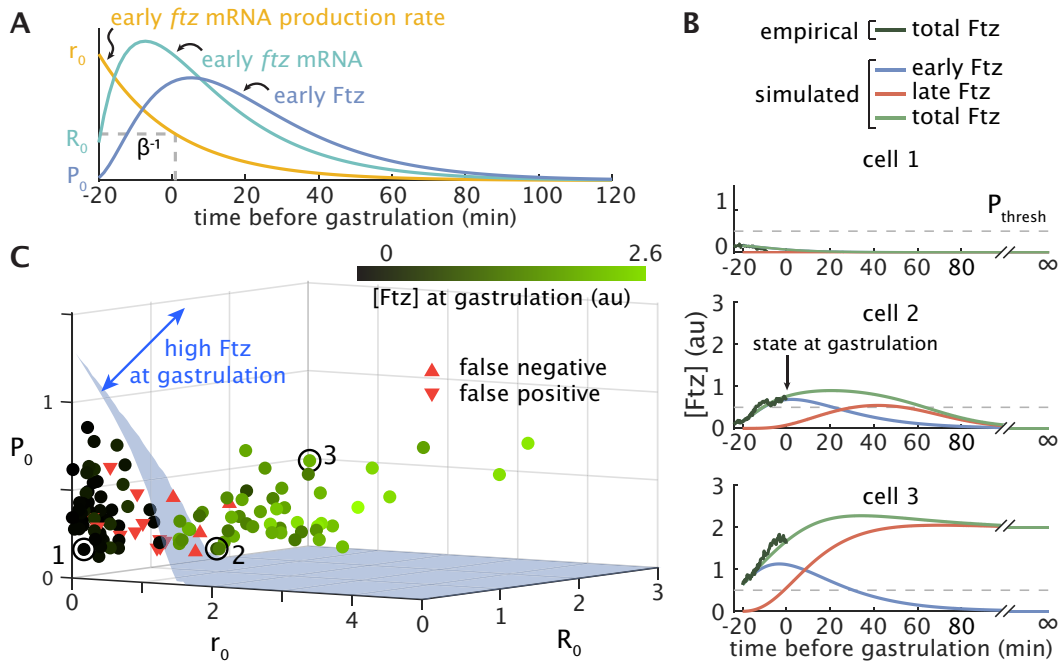


Figure 5. Mathematical modeling accurately predicts binary Ftz expression states at gastrulation. (A) Example trajectories for the mRNA production rate $r(t)$, mRNA concentration $R_{\text{early}}(t)$, and protein concentration $P_{\text{early}}(t)$ from the early element, as described by Eq. 5. (B) Representative traces for three nuclei comparing empirical total Ftz trajectories (dark green) to simulated trajectories (green) comprising contributions from both the early (blue) and autoregulatory (red) elements. Gray dashed line marks the experimentally determined threshold used to classify cells as high or low Ftz expression states at gastrulation (Figure 2D). The plotted nuclei correspond to the circled and labeled points in panel C. Note that the simulations extend well past the time that we can obtain experimental measurements. (C) Each nucleus has a set of initial conditions ($r(t_{on}) = r_0$, $R_{\text{early}}(t_{on}) = R_0$, $P_{\text{early}}(t_{on}) = P_0$) for the dynamics of the early element. The blue surface separates those nuclei (circles) that are predicted to express low levels of Ftz at gastrulation (below the surface) from those that are predicted to express high levels of Ftz (above the surface). Color intensity corresponds to the Ftz concentration at gastrulation. Downward-facing red triangles indicate false positives (predicted high at gastrulation, but experimentally determined to be low) and upward-facing red triangles indicate false negatives (predicted low, but experimentally determined to be high). Results are shown for $N = 118$ nuclei from 3 embryos at the anterior boundary of stripe 4, with model parameters given in Table S1.

the protein resulting from the autoregulatory element through the translation of the mRNA produced by this element (first term on the right-hand side) and degradation (second term on the right-hand side). Finally, as indicated in Eq. 4, we assume that the autoregulatory element is only active for $t \geq t_{on}$. We note, however, that our model produced nearly identical results whether we assumed that this transition to full responsiveness occurred instantaneously at time t_{on} , or whether we assumed a gradual increase in responsiveness over time (Section S3.1).

After time t_{on} , in addition to mathematically describing the expression dynamics of the autoregulatory element, we can also model the contribution of the early element to *fzt* expression as a dynamical system. In particular, our empirical measurements of the early element transcription rate using the MCP-MS2 system revealed that its transcription rate $r(t)$ follows an approximately exponential decay with a decay constant β^{-1} of about 21 min (Figure 3C; Figure S4; Section S2.3). We can then represent the mRNA $R_{\text{early}}(t)$ and protein $P_{\text{early}}(t)$ produced from the early module

237 using the linear system of equations

$$\begin{cases} \frac{dr}{dt} &= -\beta r(t) \\ \frac{dR_{early}}{dt} &= r(t) - \gamma_R R_{early}(t) \\ \frac{dP_{early}}{dt} &= \alpha R_{early}(t) - \gamma_P P_{early}(t), \end{cases} \quad (5)$$

238 where the equation for $\frac{dr}{dt}$ has been introduced to model the approximately exponential decay of
239 the rate of transcription of the early element after the onset time t_{on} . Here, R_{early} dynamics are
240 dictated by the transcription rate $r(t)$ and the mRNA degradation rate. The early protein P_{early} is
241 determined by the translation of the mRNA stemming from the early element as well as by protein
242 degradation. Note that, regardless of the choice of parameter values or initial conditions, $P_{early}(t)$
243 converges to 0 as t goes to infinity ([Section S1.2](#)), indicating that signaling from upstream factors
244 is transient.

245 The behavior of the *ftz* regulatory system depends crucially on the quantitative values of the ki-
246 netic rates describing the molecular interactions within our model. For those parameters that were
247 not already present in the literature, we carried out a set of experiments designed to directly mea-
248 sure these free parameters as described in detail in [Section S2](#). First, the gene regulatory function
249 $f(P)$ was measured by averaging the traces obtained from simultaneous imaging of endogenous
250 *Ftz* protein and the corresponding autoregulatory response as previously shown in [Figure 4D](#). Sec-
251 ond, the translation rate α was found by simultaneously measuring the rate of transcription and
252 the resulting protein concentration in a transgenic construct where *ftz* mRNA was labeled with MS2
253 and the resulting *Ftz* protein tagged with a LlamaTag ([Figure S3](#)). Third, the decay in the transcrip-
254 tion rate of the early element over time β was determined by fitting an exponential function to
255 the transcriptional dynamics of the early element construct ([Figure S4](#)). Fourth, the scaling factor
256 c was inferred by systematically comparing simulated to measured traces in the regime where the
257 gene regulatory function was saturated and mRNA production rate was at its maximum ([Figure S5](#)).
258 Finally, the mRNA and protein decay rates γ_R and γ_P were drawn from existing measurements in
259 the literature. All parameter values are reported in [Table S1](#).

260 If our model of the *ftz* regulatory system is accurate, then for each nucleus along the anterior
261 boundary of stripe 4, we should be able to predict *Ftz* expression state at gastrulation based only on
262 measurements at time $t_{on} = -20$ min. Specifically, at this point, each nucleus will have a different
263 initial expression rate, mRNA level, and protein level from the early module given by $r(t_{on}) = r_0$,
264 $R_{early}(t_{on}) = R_0$, and $P_{early}(t_{on}) = P_0$, respectively. The autoregulatory element, however, will not have
265 produced any mRNA or protein prior to -20 min, so the initial conditions for the autoregulatory
266 module will be $R_{late}(t_{on}) = 0$ and $P_{late}(t_{on}) = 0$.

267 Each set of initial conditions (r_0, R_0, P_0) for the early module defines a trajectory for $P_{early}(t)$
268 ([Figure 5A](#)) that will in turn drive expression from the autoregulatory module. The result is a unique
269 overall trajectory for total *Ftz* concentration $P_{total}(t) = P_{early}(t) + P_{late}(t)$ ([Figure 5B](#)) for each nucleus.
270 Hence, for a given set of initial conditions, we can simulate the full dynamical system starting at
271 t_{on} and see whether total *Ftz* concentration exceeds a threshold at gastrulation (i.e., $P_{early}(t = 0) +$
272 $P_{late}(t = 0) > P_{thresh}$, where P_{thresh} is empirically determined as shown in [Figure 2D](#)) in order to predict
273 the *Ftz* expression state of the nucleus at gastrulation. Moreover, since increasing any one of the
274 initial conditions can only increase total *Ftz*, if we plot all possible sets of initial conditions $(r_0, R_0,$
275 $P_0)$, then a single smooth surface separates the sets that result in high *Ftz* at gastrulation (above
276 the surface) from the sets that result in low *Ftz* at gastrulation (below the surface), as visualized in
277 [Figure 5C](#).

278 We used the smooth surface separating high and low *Ftz* states in our model to directly predict

279 Ftz state at gastrulation for our experimentally measured nuclei. To avoid conflating measurements with predictions, we analyzed a set of $N = 3$ embryos independently from those used to
280 obtain all model parameter values, including the gene regulatory function (**Section S2**). Our model
281 achieved 86.4% binary classification accuracy (102 of 118 nuclei) based on the system's initial con-
282 dition at $t = t_{on}$ relative to the experimentally measured Ftz expression state at gastrulation ($t = 0$)
283 determined by thresholding measured Ftz concentrations for each nucleus. The majority of classi-
284 fication errors were false negatives derived from a single embryo; excluding this embryo from anal-
285 ysis produced an overall prediction accuracy of 93.5% (72 of 77 nuclei). For the two well-predicted
286 embryos, the empirical false negative, false positive, and total error rates aligned extremely well
287 with error rates derived from stochastic simulations (**Section S3.4**). As a result, it is plausible that
288 many of the remaining classification errors can be attributed to noisy gene expression dynamics.
289

290 Taken together, these observations suggest that our simple model captures the essential de-
291 terministic components of Ftz dynamics and is able to predict Ftz expression state at gastrulation
292 from knowledge of the initial conditions of the early element. However, being able to predict Ftz
293 expression state at gastrulation does not guarantee that the autoregulatory element permanently
294 locks the Ftz expression fate for the rest of development through bistability. To determine whether
295 such developmental memory is at play, we need to further analyze our theoretical model.

296 **2.4 The *ftz* autoregulatory module is bistable and remembers binary cell state**

297 Having established that our model accurately predicts transient Ftz expression state at gastrulation,
298 we next analyzed the behavior of the early and autoregulatory modules separately, with the goal
299 of uncovering whether the autoregulatory module is bistable and, as a result, retains a long-term
300 binary memory of these Ftz levels.

301 We first performed a test of the autoregulatory module to ascertain whether it is bistable in
302 the absence of Ftz contribution from the early element ($P_{early}(t) = 0$). Such bistability would enable
303 the module to maintain a high or low expression state even once upstream regulatory factors
304 binding the early element have degraded. Following the procedure described in **Box 1** and **Section S**
305 **1.3**, we identified the steady states where mRNA and protein concentrations no longer change
306 in time. Our analysis revealed that, indeed, the empirically determined model parameters set
307 the autoregulatory module in a bistable regime (**Figure 6A**) characterized by the presence of two
308 stable steady states corresponding to low and high Ftz values. This result indicates that the *ftz*
309 autoregulatory module is capable of maintaining high or low levels of *ftz* expression indefinitely.

310 Since our model predicts that the autoregulatory element is capable of remembering Ftz ex-
311 pression levels, the question thus arises of whether the module actually becomes responsive to
312 Ftz concentration in time to lock the transient state observed in the blastoderm into a permanent
313 cell fate. Otherwise, if the bistable module becomes responsive too late, cells could transiently
314 express high Ftz at gastrulation without committing to stably expressing high Ftz in the long term.

315 To distinguish between these two scenarios, we compared the binary classification of nuclei
316 into high or low Ftz expression states at gastrulation as introduced in the previous section with the
317 final high or low expression fate predicted by the model in steady state (**Figure 6B**). Similarly to the
318 case of binary classification, the regions of parameter space (r_0 , R_0 , P_0) resulting in high fates are
319 separated from the region of parameters resulting in low fates by a surface called the switching
320 separatrix (**Sootla et al., 2016**), so named because if the initial conditions of a cell are above the
321 surface, then the bistable autoregulatory module will switch on. The initial conditions for all nuclei
322 at the anterior of stripe 4 are plotted in **Figure 6C** alongside the switching separatrix (red surface)
323 and the surface for transient binary classification of Ftz state at gastrulation (blue surface).

324 If we restrict our analysis to the “best predicted” nuclei (expression state correctly classified at
325 gastrulation and with relatively low cumulative error between simulation and empirical measure-
326 ment over time; see **Section S3.1**), 93.7% (74 of 79 nuclei) were predicted to maintain their binary

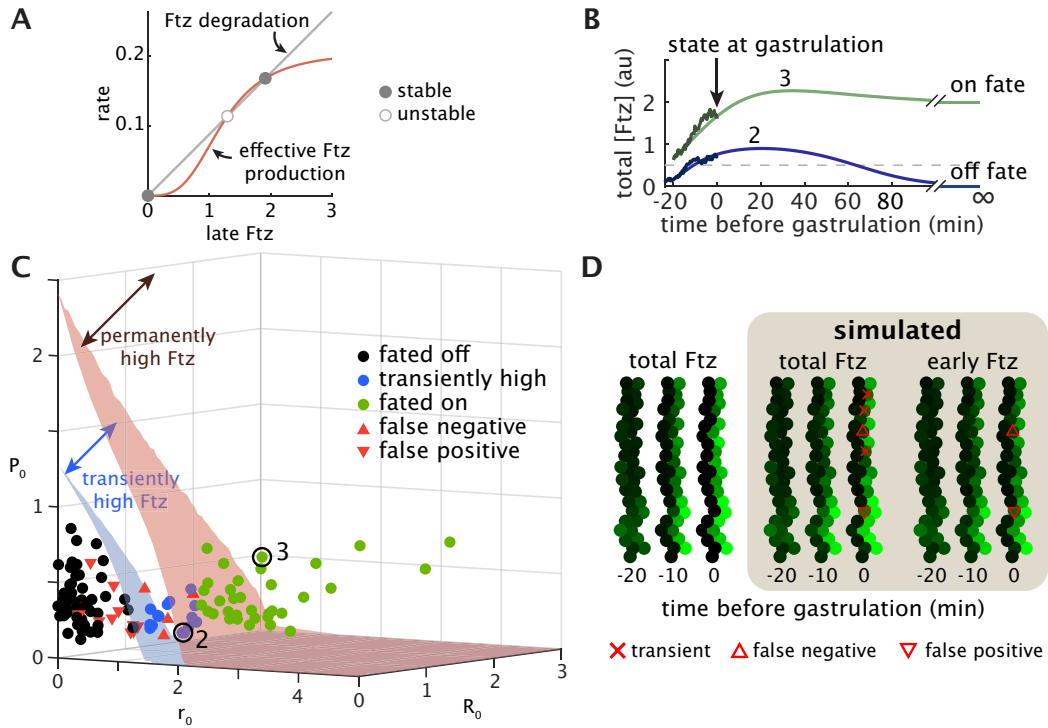


Figure 6. Quantitative mathematical model reveals that the *ftz* autoregulatory module is bistable. (A) The intersection between Ftz degradation rate and the effective Ftz production rate (i.e., late Ftz production rate adjusted for late *ftz* mRNA production and decay rates) reveals that the autoregulatory module is bistable, as described in **Box 1** and **Section S1.3**. (B) Most cells that express high Ftz state at gastrulation reach the high fate at steady state (cell 3), but some transiently express high Ftz at gastrulation before ultimately reaching the low fate (cell 2). The threshold (dashed gray line) is only used to determine state at gastrulation; fate is decided by which of the two stable steady states is approached by the system in simulation at long times. (C) The early module dictates the transient dynamics of Ftz as well as the fate it is predicted to adopt at infinite time once the autoregulatory element has reached steady state. The blue surface is repeated from **Figure 5** and separates nuclei into low (below surface) and high (above surface) Ftz state at gastrulation. The red surface (switching separatrix) separates nuclei predicted to adopt the low Ftz fate (black circles) from those predicted to adopt the high Ftz fate (green circles), where by “fate” we mean expression level at infinite time (steady state). Nuclei between the blue and red surface (blue circles) are considered transiently high in that they express high Ftz at gastrulation but are predicted to adopt the low Ftz fate. Data are plotted for $N = 118$ nuclei from 3 embryos. Red triangles indicate false negatives (upward) and false positives (downward) as determined from classification at gastrulation. (D) Results from a representative embryo show that the experimentally measured stripe pattern (left) is recapitulated by simulation (middle). A stripe pattern is still evident at gastrulation even from the predicted early Ftz concentration alone (right). Nuclear intensities at all time points are normalized to the predicted steady-state high Ftz concentration. Red “x”s denote nuclei with a transiently high Ftz state at gastrulation; triangles denote false positives (downward) and false negatives (upward). Parameters for simulation are as given in **Table S1**.

327 state and adopt the corresponding Ftz expression fate in steady state, as exemplified by cell 3 in
328 **Figure 6B**. The remaining 6.3% of nuclei (5 of 79), despite having a high Ftz expression state at gas-
329 trulation, were predicted to drop to a low Ftz fate in steady state as shown by cell 2 in **Figure 6B**.
330 No nuclei classified as low Ftz expression state at gastrulation were predicted to express high Ftz
331 after gastrulation. Thus, the autoregulatory element ensures that the vast majority of cells adopt
332 a fate matching the transient state at gastrulation.

333 While it is clear that the autoregulatory element establishes developmental memory by fixing
334 the Ftz expression fate in steady state, we wondered whether this memory was already at play
335 at gastrulation, or whether the early module is principally responsible for setting Ftz state at gas-
336 trulation. Our simulations show that a stripe pattern is already evident at gastrulation from the
337 contribution of the early protein alone, ignoring the autoregulatory contribution (**Figure 6D**). Thus,
338 it appears that the anterior boundary of stripe 4 at gastrulation is defined by the regulatory activ-
339 ity of upstream factors binding the early element in a manner that is largely independent of the
340 activity of the autoregulatory element. Therefore, this result supports the conclusion that the au-
341 toregulatory module is bistable and that it primarily serves to commit cells to fates predetermined
342 by the early element.

343 **2.5 Ftz fate is robustly specified in half an hour**

344 Given that the *ftz* autoregulatory element acts as a memory module, we might ask how long it takes
345 nuclei to convert the transient expression state of the early module into a stable cellular memory,
346 thereby establishing an expression fate at long times beyond gastrulation. We posit that this times-
347 pan corresponds to the classical notion of a commitment window, defined as the period of time
348 during which a cell integrates information from external factors to decide its fate ([Dalton, 2015](#);
349 [McNeely and Dwyer, 2021](#)). It can be difficult to access temporal features of development such as
350 the commitment window *in vivo*, in part due to the technical challenge of measuring and system-
351 atically manipulating input signals while simultaneously monitoring the resulting gene expression
352 programs in individual cells within intact tissues or organisms ([Bending et al., 2018](#); [Johnson and](#)
353 [Toettcher, 2018](#)).

354 Our mathematical model provided us with a unique opportunity to examine the commitment
355 window by altering the timing of developmental events *in silico*. Because the low Ftz fate at steady
356 state is the default expression state—the autoregulatory module will always produce zero protein
357 in the absence of a transient signal from the early module—the commitment window primarily
358 determines whether the cell has enough time to detect if transient Ftz concentrations are high
359 and, if so, to adopt a trajectory destined for a high steady-state expression fate. Thus, for the
360 results reported in this section, we restricted our analysis to a subset of the best predicted nuclei,
361 the nuclei that were correctly classified at gastrulation and have relatively low cumulative error
362 between simulation and experiment over time ([Section S3.1](#)), that were also predicted to adopt
363 the high fate according to the switching separatrix analysis ($N = 21$; **Figure 6B**).

364 We define the commitment window as $t_{off} - t_{on}$, where t_{on} indicates the start of autoregulatory
365 responsiveness and t_{off} is the time when upstream factors stop controlling the transcriptional dy-
366 namics of the early element (**Figure 7A** and B). In other words, the commitment window represents
367 the total amount of time during which both the early and autoregulatory modules dictate *ftz* ex-
368 pression (**Figure 7C**), and serves as an estimate for how long the autoregulatory module has to
369 establish a memory of transient Ftz state. We define t_{off} such that $r(t \geq t_{off}) = 0$, where $r(t)$ is the
370 mRNA production rate of the early element. Before t_{off} , $r(t)$ follows the usual exponential decay
371 with rate $1/\beta = 21$ min (**Figure 7B**).

372 To determine how long of a commitment window allows cells to convert transiently high Ftz
373 concentrations into permanently high Ftz fates, we asked whether our analyzed subset of nuclei
374 still reached the high fate as we systematically varied the commitment window. We solved the

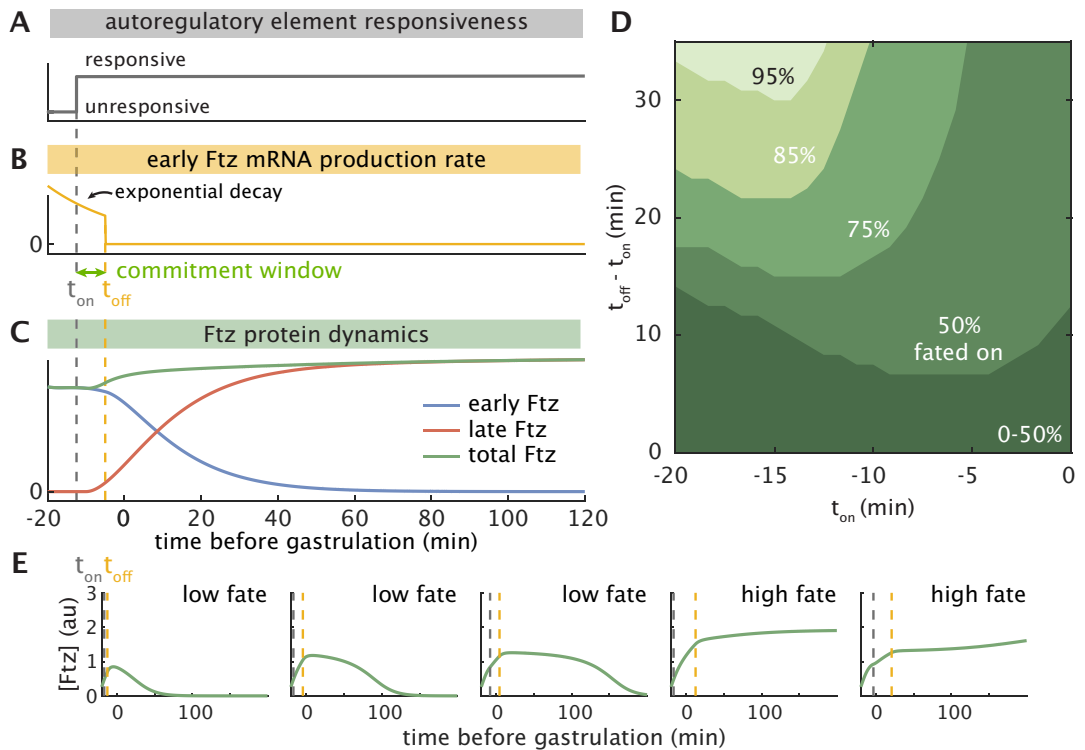


Figure 7. In silico analysis reveals the window of commitment of cells to the high Ftz fate. (A-B)
 Schematic illustrating (A) t_{on} , the time the autoregulatory element becomes responsive, and (B) t_{off} , the time the early element ceases production. The commitment window $t_{off} - t_{on}$ is the timespan during which both upstream factors and autoactivation dictate Ftz expression, and serves as an estimate for how long the autoregulatory module has to establish a memory of the signal from the early module. (C) Simulated Ftz concentrations resulting from the timing pictured in A and B. (D) Contour plot showing what percentage of the subset of analyzed nuclei (see text) reach high Ftz fate under wild-type conditions ($N = 21$; [Figure 6B](#), [Section S3.1](#)) still reach that fate as the commitment window $t_{off} - t_{on}$ is varied and t_{on} is delayed relative to the measured -20 min (see text). (E) Simulated single-nucleus traces of total Ftz for varying values of t_{on} and the commitment window can cause the transient dynamics to vary quite dramatically. Dashed lines denote the t_{off} (gold) and t_{on} (gray) values used for each plot. Parameters are as in [Table S1](#). See also [Figure S10](#).

375 dynamical system from **Eq. 4** and **Eq. 5** with commitment windows of increasing length and start
376 times t_{on} between -20 min and 0 min and recorded which nuclei reached the high Ftz fate. Our
377 results are reported in terms of the fraction of nuclei within the subset that adopted the high Ftz
378 fate for each timing condition.

379 **Figure 7D** shows the fraction of nuclei predicted to adopt the high Ftz fate as a function of
380 the commitment window and t_{on} . For example, assuming $t_{on} \leq -13$ min, a commitment window
381 of 34 min results in 95% of nuclei achieving high steady-state Ftz levels without further signaling
382 from the early element (**Figure 7D**). Our results also reveal that there is a gradual dropoff in the
383 fraction of cells that do not commit to the high fate as the commitment window is shortened or
384 t_{on} is delayed. This suggests that slight temporal perturbations during development are unlikely to
385 cause catastrophic patterning failures in which all cells suddenly adopt the low Ftz fate. Rather, we
386 might expect small changes in timing to affect the fates of only a small percentage of cells.

387 Our analysis of the commitment window indicates that about half an hour can suffice for the
388 vast majority of high-fated cells to stably commit to that fate. Proper fate specification, however,
389 does not guarantee similarity in the temporal trajectories of Ftz concentration, as evidenced by the
390 wide range of dynamics observed in simulated traces for varying t_{on} and t_{off} with the same initial
391 conditions for the early module (**Figure 7E**; **Figure S10**). Thus, if the transient Ftz trajectory, not
392 just its ultimate fate, is instructive for downstream genes, then the need for proper regulation of
393 these genes may place stricter constraints on the relative timing of the early and autoregulatory
394 elements than those that are imposed by the specification of steady state Ftz fate alone.

395 **3 Discussion**

396 For decades, developmental biologists have used the concept of Waddington's landscape to con-
397 ceptualize the adoption of discrete cell fates. Under this framework, cells roll down valleys in
398 a predetermined landscape to adopt their ultimate fates. This framework has been repeatedly
399 mathematized using dynamical systems theory ([Wang et al., 2011](#); [Furusawa and Kaneko, 2012](#);
400 [Jaeger and Monk, 2014](#); [Corson and Siggia, 2017](#); [Sáez et al., 2022](#)). Many of these studies have
401 hypothesized that positive autoregulation ([Crews and Pearson, 2009](#)) helps establish and maintain
402 binary cell fates through bistability ([Zernicka-Goetz et al., 2009](#); [Soldatov et al., 2019](#)), which can
403 be thought of as introducing forks in Waddington's landscape. Though experiments in cell cul-
404 ture and fixed tissue have provided evidence for the bistability of various autoregulatory modules
405 found within gene regulatory networks, until now, these results have not been confirmed by direct
406 examination of dynamics in intact, living embryos.

407 In this work, we utilized live imaging approaches to quantitatively characterize the dynamics of
408 the fruit fly *ftz* regulatory system *in vivo*. We elucidated tight temporal coordination between the
409 two enhancer elements that regulate *ftz* expression (**Figure 3**), and combined dynamical systems
410 modeling with biophysical measurements to show that the bistability of the autoregulatory module
411 can remember otherwise transient expression levels driven by upstream factors (**Figure 6**). Based
412 on the prevalence of autoregulatory motifs found in nature ([Alon, 2006](#); [Peter and Davidson, 2015](#)),
413 we speculate that the approach employed by the Ftz system to decide cell fate is not limited to fruit
414 flies, but might also be widely adopted during development in other organisms.

415 One of our central discoveries is that *ftz* autoregulation is triggered at a specific developmental
416 time rather than by a threshold concentration of Ftz protein driven by the early element. Recent
417 work has suggested candidates for "timer genes" that are expressed at distinct developmental time
418 points and appear to facilitate the expression of other genes ([Clark and Akam, 2016](#); [Clark and Peel,](#)
419 [2018](#); [Clark et al., 2022](#)). At least one of these timer genes, Odd-paired, has been shown to exhibit
420 chromatin opening activity ([Soluri et al., 2020](#)), and two, Caudal and Dichaete, have been shown to
421 bind directly to the eve autoregulatory element ([MacArthur et al., 2009](#)). We speculate that timer

422 genes might also bind the *ftz* autoregulatory element to trigger its responsiveness to Ftz protein.
423 Furthermore, the tight temporal coordination we observed between the transcriptional activity
424 driven by the early and autoregulatory elements suggests that sequentially expressed timer genes
425 might differentially regulate enhancers to precisely coordinate gene expression during develop-
426 ment.

427 A basic assumption of our work is that genetic networks exhibit modularity ([Hartwell et al., 1999](#);
428 [Bolouri and Davidson, 2002](#); [Del Vecchio et al., 2016](#)), meaning the network can be broken
429 down into parts (modules), each with some inputs and outputs connected to other modules. The
430 behavior of the whole network can then be predicted from the behavior of the modules in isolation.
431 How to define the modules, or equivalently how to break the network down into parts, has been
432 the subject of much discussion ([Hartwell et al., 1999](#)). As we have argued in this work, topology,
433 the pattern of interactions among molecular species, is not enough to determine the behavior
434 of a module. Indeed, its dynamics will depend on the values of the parameter governing these
435 interactions ([Angeli et al., 2004](#); [Ingram et al., 2006](#); [Graham et al., 2010](#); [Blanchini and Franco,](#)
436 [2014](#); [Khammash, 2016](#); [Verd et al., 2019](#)).

437 There is inherent flexibility in deciding which physical components to include in a module, and
438 hence which quantities act as parameters and which as inputs to the module. For example, for
439 the *ftz* autoregulatory system, the distinction between the early and autoregulatory elements led
440 us to structure the autoregulatory module with input P_{early} and output P_{late} [Figure S2](#). This is not
441 the only way to define the module; notably, if we knew which regulatory factors rendered the
442 autoregulatory element responsive, then we could include those as inputs and modify the model
443 accordingly.

444 Our fairly simple representation of the autoregulatory module can predict the fate of *ftz* expres-
445 sion from arbitrary trajectories of early Ftz. As a result, we can predict the effect of modifications
446 to upstream signaling on the resulting gene expression patterns. This, in turn, allows us to ask
447 what forms of input are appropriate to achieve particular patterning outcomes. Such ability to
448 reverse engineer the process of cellular decision-making could facilitate designing perturbations
449 to manipulate the system, identifying constraints placed on upstream modules by the needs of
450 downstream modules, and analyzing whether biologically evolved signals match those that are
451 mathematically “optimal” for such needs as speed of patterning ([Pezzotta and Briscoe, 2022](#)) or
452 information transmission ([Tkačík and Gregor, 2021](#)). Different methods of generating predictions
453 may be appropriate depending on the types of inputs under consideration. In this paper, the fact
454 that increasing any one of the parameters that define the early Ftz input (r_0 , R_0 , P_0) increases to-
455 tal Ftz concentration at all points in time (a property known as monotonicity; [Angeli et al. \(2004\)](#);
456 [Sootla et al. \(2016\)](#)) made it possible to analyze our model using a switching separatrix. However,
457 this may not be true for other regulatory systems, as in the case where a gene within a module
458 represses its own production.

459 Throughout developmental biology, the concept of a commitment window has been repeatedly
460 utilized to describe the amount of time cells need to be exposed to upstream signals in order to de-
461 cide their developmental fates ([Dalton, 2015](#); [McNeely and Dwyer, 2021](#)). Our quantitative dynami-
462 cal systems model made it possible to conduct a detailed examination of this commitment window,
463 and to identify what fraction of cells adopt certain fates as developmental timing is varied. From
464 an engineering perspective, we may consider a gene expression pattern as a “design specification”
465 that must be achieved with a prescribed level of precision, and work backwards to see what inputs
466 satisfy this requirement. Our approach complements existing work on precision that emphasizes
467 how tightly protein concentrations are controlled ([Gregor et al., 2007](#)) and how accurately cells
468 can locate their position by reading out concentrations of upstream factors ([Dubuis et al., 2013](#);
469 [Petkova et al., 2019](#)). In particular, the latter approaches indicate what level of precision is actually

470 achieved by a patterning network, while our framing focuses rather on what range of parameters al-
471 low a system to attain a predefined level of precision. A combination of the two perspectives could
472 help elucidate what biophysical and evolutionary factors influence stochastic variation in pheno-
473 types, including how precise expression patterns must actually be to produce functional, healthy
474 organisms. In any case, we hope our results act as one more step toward grounding robustness
475 or reproducibility in developmental patterning on a quantitative, probabilistic level.

476 In summary, by turning widespread schematic models of autoactivation modules into precise
477 mathematical statements and experimentally testing the resulting predictions, we have provided
478 support for a widely held hypothesis about how developmental fates are established in embryos.
479 In the future, combining quantitative measurements with precise spatiotemporal perturbations
480 ([Goglia and Toettcher, 2019](#)) and synthetic reconstitution methods ([McNamara et al., 2022](#)) promises
481 to enable yet another iteration of the dialogue between theory and experiment that constitutes the
482 basis of our work, ultimately leading to a predictive understanding of function in developmental
483 networks and the myriad forms and fates to which they give rise.

484 Methods and Materials

485 Cloning and Transgenesis

486 The fly lines used in this study were generated by inserting transgenic reporters into the fly genome
487 or by CRISPR-Cas9 genome editing, as described below. See **Table S2** for detailed information on
488 the plasmid sequences used in this study.

489 Creation of tagged *fushi tarazu* (*ftz*) gene using CRISPR-Cas9

490 Ftz-EGFP-LlamaTag fusion design is based on previously published transgenic line (**Bothma et al.,**
491 **2018**). To tag endogenous *ftz* locus with EGFP-LlamaTag, we used CRISPR-mediated homology-
492 directed repair with donor plasmid synthesized by Genscript. gRNA was designed using the target
493 finder tool from flyCRISPR (<https://flycrispr.org>), and cloned based on the protocol from **Gratz et al.**
494 (**2015**). *yw;nos-Cas9(II-attP40)* transgenic line was used as the genomic source for Cas9 and the
495 embryos were injected and screened by BestGene Inc.

496 Creation of *ftz* autoregulatory element reporter

497 The *ftz* autoregulatory element sequence is based on 4.4kb DNA segment described in (**Hiromi**
498 **et al., 1985**). The *ftz* autoregulatory element reporter was constructed by combining the enhancer
499 sequence with an array of 24 MS2 stem loops fused to the *D. melanogaster yellow* gene (**Bothma**
500 **et al., 2018**). The construct was synthesized by Genscript and injected by BestGene Inc into *D.*
501 *melanogaster* embryos with a Φ C31 insertion site in chromosome 3 (Bloomington stock #9750;
502 landing site VK00033; cytological location 65B2).

503 Transgenes expressing EGFP and MCP-mCherry

504 The fly line maternally expressing MCP-mCherry (chromosome 3) was constructed as described
505 in (**Bothma et al., 2018**). The fly line maternally expressing vasa-EGFP (chromosome 2) was con-
506 structed as described in (**Kim et al., 2021**). To simultaneously image protein dynamics using Lla-
507 maTags and transcription using MCP-MS2 system, we combined the vasa-EGFP transgene with
508 MCP-mCherry to construct a new line (*yw;vasa-EGFP;MCP-mCherry*) that maternally expresses both
509 proteins.

510 Fly lines

511 To measure Ftz transcription and protein levels simultaneously, we performed crosses to gener-
512 ate virgins carrying transgenes that drive maternal EGFP, MCP-mCherry, the LlamaTagged Ftz locus
513 along with *ftz* autoregulatory element reporter (*yw; vasa-EGFP; MCP-mCherry*).
514 These flies were then crossed with males having both the *ftz* autoregulatory element reporter and
515 the LlamaTagged Ftz locus (*yw; +; FtzAuto-MS2-Yellow, Ftz-LlamaTag*). This resulted in the embryo
516 carrying maternally deposited EGFP, MCP-mCherry, and two copies of the LlamaTagged Ftz locus
517 and *ftz* autoregulatory element reporter.

518 Embryo preparation and data collection

519 The embryos were prepared following procedures described in (**Garcia et al., 2013; Bothma et al.,**
520 **2018; Lammers et al., 2020**). Embryos were collected and mounted in halocarbon oil 27 between
521 a semipermeable membrane (Lumox film, Starstedt, Germany) and a coverslip. Confocal imaging
522 on a Zeiss LSM 780 microscope was performed using a Plan-APOCHROMAT 40x /1.4NA oil immersion
523 objective. EGFP and MCP-mCherry were excited with laser wavelengths of 488 nm (25.0 μ W laser
524 power) and 594 nm (15.0 μ W laser power), respectively. Fluorescence was detected using the Zeiss
525 QUASAR detection unit. Image resolution was 512 \times 512 pixels, with pixel size of 0.231 μ m. Se-
526 quential z-stacks separated by 0.5 μ m were acquired. Specimens were imaged from mid nuclear
527 cycle 14 until the start of gastrulation.

528 **Image processing**

529 Image analysis of live embryo movies was performed based on the protocol in ([Garcia et al., 2013](#);
530 [Reimer et al., 2021](#)), which included nuclear segmentation, spot segmentation, and tracking. In
531 addition, the nuclear fluorescence of Ftz was calculated based on a nuclear mask generated from
532 the MCP-mCherry channel. Ftz concentration for individual nuclei was extracted based on the inte-
533 grated amount from maximum projection along the z-stack. The GFP background was calculated
534 based on a control experiment and subsequently subtracted from the data.

535 **Numerical analysis and simulations**

536 Numerical analysis and simulations were carried out using custom scripts in MATLAB (2017b). The
537 switching separatrix and analogous surface for transient Ftz state at gastrulation were estimated
538 using a modification of the algorithm in ([Sootla et al. \(2016\)](#)), which employs a combination of bi-
539 section and random sampling to estimate the upper and lower bounds of the separatrix surface.
540 Stochastic differential equations were simulated using the Euler-Maruyama method. More detailed
541 descriptions of the procedures are available in the Supplementary Text.

542 **Acknowledgments**

543 MLP was supported by the European Molecular Biology Laboratory Interdisciplinary Postdoc Pro-
544 gramme (EIPOD4 fellowships), cofunded by Marie Skłodowska-Curie Actions (grant agreement num-
545 ber 847543). HGG was supported by the Burroughs Wellcome Fund Career Award at the Scien-
546 tific Interface, the Sloan Research Foundation, the Human Frontiers Science Program, the Searle
547 Scholars Program, the Shurl and Kay Curci Foundation, the Hellman Foundation, the NIH Direc-
548 tor's New Innovator Award (DP2 OD024541-01), NSF CAREER Award (1652236), an NIH R01 Award
549 (R01GM139913) and the Koret-UC Berkeley-Tel Aviv University Initiative in Computational Biology
550 and Bioinformatics. HGG is also a Chan Zuckerberg Biohub Investigator.

551 **Author contributions**

552 Conceptualization: JZ, MLP, HGG
553 Methodology: JZ, MLP, HGG
554 Resources: JZ, MLP, MN, HGG
555 Investigation: JZ, MLP, HGG
556 Visualization: JZ, MLP, HGG
557 Funding acquisition: HGG
558 Project administration: HGG
559 Supervision: HGG
560 Writing – original draft: JZ, MLP, HGG
561 Writing – review & editing: JZ, MLP, HGG

562 **Declaration of interests**

563 The authors declare no competing interests.

564 **Data and materials availability**

565 All materials are available upon request. All data in the main text or supplementary materials are
566 available upon request. All code is available in this paper's [github repository](#).

567 Supplementary Information

568 Supplementary Figures

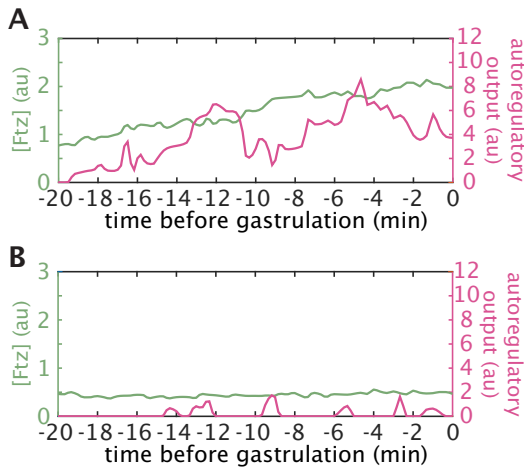


Figure S1. Single-cell traces of Ftz protein and autoregulatory activity show that high or low Ftz concentration results in distinct temporal dynamics. Green and magenta lines correspond to Ftz protein and transcriptional activity of the autoregulatory element, respectively, obtained as described in fig:autoregulationA. **(A)** High level of Ftz protein results in continued active transcription from the autoregulatory element. **(B)** Low level of Ftz protein results in a much weaker autoregulatory response.

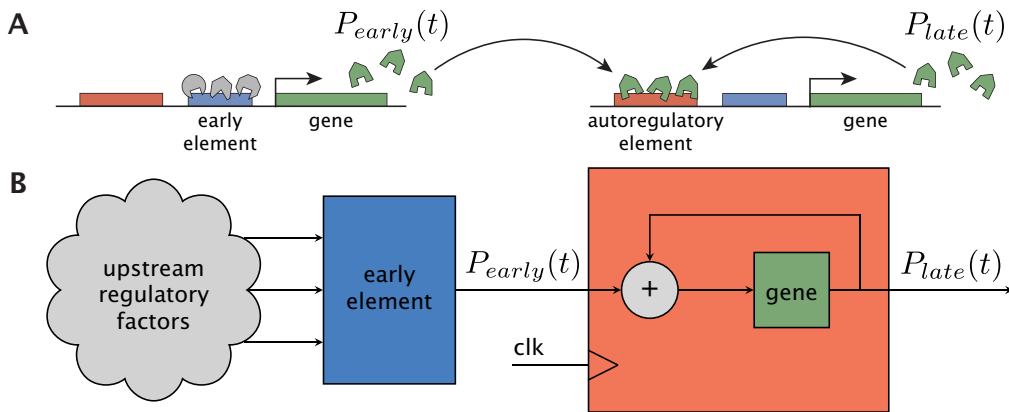


Figure S2. Two ways to visualize a genetic network as an interconnection of modules. (A) Schematic of Ftz regulation in which populations of Ftz protein are differentially labeled based on whether they are generated by regulation from the early element ($P_{early}(t)$) or from the autoregulatory element ($P_{late}(t)$). The two populations are summed to generate the total Ftz concentration that binds the autoregulatory element. (B) The Ftz regulatory system can be visualized as a block diagram to highlight how a modular network decomposition might be inspired by similar breakdowns of electrical circuits and other engineering control systems (Cosentino and Bates, 2011). Here, unspecified upstream factors regulate the early element module, which produces output $P_{early}(t)$. This, in turn, acts as the input to the autoregulatory module, which has been schematized as a latch with a clock signal (clk) to show that the element only becomes responsive at a particular time. The output $P_{late}(t)$ can be summed with $P_{early}(t)$ to recover total Ftz concentration. Relative to the more traditional schematic in (A), this representation includes dynamic signals ($P_{early}(t)$ and $P_{late}(t)$), a timing element that triggers autoregulatory responsiveness, and a clear separation of inputs and outputs from each module.

⁵⁶⁹ **Supplementary Tables**

Table S1. Quantitative parameters used throughout this work

Parameter	Description	Source	Value	Units
α	translation rate	this work	0.082 ± 0.004	protein AU (mRNA AU min) ⁻¹
τ_R	mRNA half-life	(Edgar et al., 1986)	7	min
γ_R	mRNA decay rate	$\frac{\ln 2}{\tau_R}$	0.0990	min ⁻¹
τ_P	protein half-life	(Bothma et al., 2018)	7.9	min
γ_P	protein decay rate	$\frac{\ln 2}{\tau_P}$	0.0877	min ⁻¹
$f(P)$	autoactivation gene regulatory function	this work	$\frac{aP^n}{K^n + P^n}$	mRNA AU (protein AU) ⁻¹
a	maximum transcription rate	this work	$5.555e5 \times 10^5$	mRNA AU (protein AU) ⁻¹
K	-	this work	1.216×10^6	protein AU
n	Hill coefficient	this work	3.264	(none)
c	ratio of transcription rate endogenous to transgene	this work	0.45 ± 0.02	(none)
β	decay rate of early mRNA production	this work	0.0479 ± 0.0021	min ⁻¹

Table S2. List of plasmids used in this study.

Name	Function
pBPhi-FtzEarly-MS2	<i>ftz</i> early element MS2 reporter
pBPhi-FtzUpstream-MS2-Yellow	<i>ftz</i> autoregulatory element MS2 reporter
pUC57-Ftz-LlamaTag-dsRed	Donor plasmid for Ftz-LlamaTag CRISPR knock-in fusion
pU6-3-gRNA-Ftz-1	guide RNA 1 for Ftz-LlamaTag CRISPR knock-in fusion
pU6-3-gRNA-Ftz-2	guide RNA 2 for Ftz-LlamaTag CRISPR knock-in fusion
pU6-3-gRNA-Ftz-3	guide RNA 3 for Ftz-LlamaTag CRISPR knock-in fusion

⁵⁷⁰ **Supplementary Movie**

⁵⁷¹ **Movie S1.** Two-color imaging of input Ftz protein concentration and the output autoregulatory dynamics at stripes 3, 4 and 5.

573 Supplementary Text

574 S1 Modeling

575 S1.1 Autoregulatory element

576 We use $R_{early}(t)$ to describe the concentration of *ftz* mRNA transcribed from the early element, which
577 is translated into protein $P_{early}(t)$. We define $R_{late}(t)$ as the *ftz* mRNA transcribed from the autoregu-
578 latory element and translated into protein $P_{late}(t)$. The total *Ftz* protein in the cell at time t is given
579 by $P_{total}(t) = P_{early}(t) + P_{late}(t)$. The dynamical equations describing the temporal evolution of mRNA
580 and protein are

$$\text{autoregulatory element: } \begin{cases} \frac{dR_{late}}{dt} = c\tilde{f}(t, P_{total}(t)) - \gamma_R R_{late}(t), \\ \frac{dP_{late}}{dt} = \alpha R_{late}(t) - \gamma_P P_{late}(t) \end{cases}, \quad (S1)$$

581 where γ_R and γ_P are the decay rates of mRNA and protein respectively, α is the translation rate,
582 and c is a scaling factor equivalent to the ratio of maximum production rate from the endogenous
583 locus vs. the transgene (where \tilde{f} is measured). Note that $\tilde{f}(t, \cdot)$, the gene regulatory function for
584 the autoregulatory element, is time dependent. Unless otherwise stated, we will assume

$$\tilde{f}(t, P) = \begin{cases} 0, & t < t_{on}, \\ f(P), & t \geq t_{on} \end{cases}, \quad (S2)$$

585 where

$$f(P) = \frac{aP^n}{K^n + P^n} + l \quad (S3)$$

586 is the sigmoid describing the autoregulatory relationship at maximum amplitude. Using the defi-
587 nition of $P_{total}(t)$ we will then write **Eq. S1** as

$$\text{autoregulatory element: } \begin{cases} \frac{dR_{late}}{dt} = cf(P_{early}(t) + P_{late}(t)) - \gamma_R R_{late}(t), \\ \frac{dP_{late}}{dt} = \alpha R_{late}(t) - \gamma_P P_{late}(t) \end{cases}, t \geq t_{on}. \quad (S4)$$

588 Thus, $P_{early}(t)$ acts as the sole time-varying input to the autoregulatory element. Since autoregu-
589 lation does not begin until time t_{on} , the initial conditions for **Eq. S4** are fixed at $R_{late}(t_{on}) = 0$ and
590 $P_{late}(t_{on}) = 0$.

591 S1.2 Early element

592 From our empirical measurements, we observed that the production rate $r(t)$ of early *ftz* mRNA is
593 well approximated by an exponential decay (**Figure S4**), allowing us to model $R_{early}(t)$ and $P_{early}(t)$
594 through the dynamical system

$$\begin{cases} \frac{dr}{dt} = -\beta r(t) \\ \frac{dR_{early}}{dt} = r(t) - \gamma_R R_{early}(t) \\ \frac{dP_{early}}{dt} = \alpha R_{early}(t) - \gamma_P P_{early}(t) \end{cases}. \quad (S5)$$

595 As before, α is the translation rate and γ_R and γ_P are the decay rates of mRNA and protein.

596 Because **Eq. S5** is linear, it can be equivalently written as

$$\frac{d\vec{x}(t)}{dt} = \begin{bmatrix} -\beta & 0 & 0 \\ 1 & -\gamma_R & 0 \\ 0 & \alpha & -\gamma_P \end{bmatrix} \vec{x}(t) =: \mathbf{A}\vec{x}(t), \quad (S6)$$

⁵⁹⁷ where

$$\vec{x}(t) = \begin{bmatrix} r(t) \\ R_{early}(t) \\ P_{early}(t) \end{bmatrix}. \quad (S7)$$

⁵⁹⁸ The analytical solution is then given by

$$\vec{x}(t) = c_1 e^{\lambda_1 t} \vec{v}_1 + c_2 e^{\lambda_2 t} \vec{v}_2 + c_3 e^{\lambda_3 t} \vec{v}_3, \quad (S8)$$

⁵⁹⁹ where $\lambda_1, \lambda_2, \lambda_3$ are the eigenvalues of A corresponding to eigenvectors $\vec{v}_1, \vec{v}_2, \vec{v}_3$ respectively. In
⁶⁰⁰ particular,

$$\vec{x}(t) = \begin{bmatrix} 1 \\ \frac{1}{\gamma_R - \beta} \\ \frac{\alpha}{(\gamma_R - \beta)(\gamma_P - \beta)} \end{bmatrix} c_1 e^{-\beta t} + \begin{bmatrix} 0 \\ 1 \\ \frac{\alpha}{\gamma_P - \gamma_R} \end{bmatrix} c_2 e^{-\gamma_R t} + \begin{bmatrix} 0 \\ 0 \\ 1 \end{bmatrix} c_3 e^{-\gamma_P t} \quad (S9)$$

⁶⁰¹ where

$$c_1 = r(t_{on}), \quad c_2 = \left(R_{early}(t_{on}) - \frac{r(t_{on})}{\gamma_R - \beta} \right), \quad c_3 = P_{early}(t_{on}) - \frac{\alpha}{\gamma_P - \gamma_R} c_2 - \frac{\alpha}{(\gamma_R - \beta)(\gamma_P - \beta)} c_1. \quad (S10)$$

⁶⁰² Thus, the input $P_{early}(t)$ to the autoregulatory element is completely characterized by three parameters ($r(t_{on}), R_{early}(t_{on}), P_{early}(t_{on})$) corresponding to the initial conditions for **Eq. S5**. Since every term
⁶⁰³ in the solution is multiplied by an exponential that decays in time, all state variables will tend to 0
⁶⁰⁴ as t goes to infinity.

⁶⁰⁶ S1.3 Intersection test for bistability

⁶⁰⁷ In **Box 1** in the main text we give an example of how to identify stable steady states in a model that
⁶⁰⁸ only acknowledges protein concentration and ignores mRNA dynamics. Here, we show how to use
⁶⁰⁹ the graphical intersection test on systems including both mRNA and protein.

⁶¹⁰ To reiterate, our dynamical system is described by **Eq. S4** is given by

$$\text{autoregulatory element: } \begin{cases} \frac{dR_{late}}{dt} = cf(P_{early}(t) + P_{late}(t)) - \gamma_R R_{late}(t) \\ \frac{dP_{late}}{dt} = \alpha R_{late}(t) - \gamma_P P_{late}(t) \end{cases}, \quad t \geq t_{on}. \quad (S11)$$

⁶¹¹ Steady states are system states at infinite time. Since we know that $P_{early}(t)$ goes to 0 at long
⁶¹² times, the steady states for **Eq. S4** are equivalent to the steady states of

$$\text{autoregulatory element: } \begin{cases} \frac{dR_{late}}{dt} = cf(P_{late}(t)) - \gamma_R R_{late}(t) \\ \frac{dP_{late}}{dt} = \alpha R_{late}(t) - \gamma_P P_{late}(t) \end{cases}, \quad (S12)$$

⁶¹³ which has no input and can therefore be analyzed for steady states by standard methods.

⁶¹⁴ By definition, at steady state the derivative of the different molecules species with respect to
⁶¹⁵ time equals zero, allowing us to write

$$\text{autoregulatory element: } \begin{cases} 0 = cf(P_{late}^*) - \gamma_R R_{late}^* \\ 0 = \alpha R_{late}^* - \gamma_P P_{late}^* \end{cases} \quad (S13)$$

⁶¹⁶ where (R_{late}^*, P_{late}^*) is a steady state. Then, we rearrange the bottom equation to get

$$R_{late}^* = \frac{\gamma_P}{\alpha} P_{late}^*, \quad (S14)$$

⁶¹⁷ which we plug into the top equation to get

$$0 = cf(P_{late}^*) - \frac{\gamma_R \gamma_P}{\alpha} P_{late}^*. \quad (S15)$$

618 From here, we rearrange terms to recover

$$\gamma_P P_{late}^* = \frac{\alpha c}{\gamma_R} f(P_{late}^*). \quad (\text{S16})$$

619 Hence, the intersections of a line of slope γ_P with the right-hand side give the steady-state late
620 protein concentrations P_{late}^* , from which we can recover R_{late}^* through [Eq. S14](#). For a plot of the
621 intersection test, see [Figure 6A](#) in the main text.

622 S2 Parameter estimation

623 S2.1 Regulatory function $f(P)$ of the *ftz* autoregulatory element

624 We calculated the regulatory function ($f(P)$) of the *ftz* autoregulatory element (shown in [Figure 4D](#))
625 for the anterior boundary of stripe 4. To make this possible, we identified the boundary in a man-
626 ually selected image frame prior to gastrulation by extracting two adjacent columns of cells, each
627 corresponding to high or low *Ftz* concentration. For each cell, we obtained the MS2 signal, which is
628 a proxy for the instantaneous rate of transcription ([Garcia et al., 2013; Bothma et al., 2014; Lam-](#)
629 [mers et al., 2020](#)), and the *Ftz* fluorescence for each time point. Next, we binned data points within
630 a specific temporal window into ten quantiles. We averaged the MS2 and *Ftz* signals belonging to
631 the same quantile, then fit a Hill function to the resulting values to obtain the regulatory function
632 of the *ftz* autoregulatory element within that time window. We repeated the process in $N = 7$ em-
633 bryos and pooled data from all embryos for subsequent analysis over four temporal windows (-20
634 to -15, -15 to -10, -10 to -5, and -5 to 0 min) to obtain the trend shown in [Figure 4E](#).

635 S2.2 Translation rate α

636 To calculate the translation rate, we simultaneously imaged the *ftz* transcription rate and the re-
637 sulting *Ftz* protein concentration in a *Ftz*-MS2-LlamaTag construct ([Figure S3A](#)). We focused on the
638 nuclei with no initial *Ftz* transcription. For these nuclei, we measured the MS2 signal (see [Figure S3B](#)
639 for a sample trace), which is an approximation of the *ftz* mRNA production rate ([Garcia et al., 2013;](#)
640 [Lammers et al., 2020; Bothma et al., 2018](#)), and integrated this signal in order to obtain the total
641 amount of mRNA produced (see [Figure S3C; Garcia et al. \(2013\)](#)). This integration was done by
642 solving the differential equation for the mRNA $R(t)$ given by

$$\frac{dR}{dt} = r(t) - \gamma_R R(t), \quad (\text{S17})$$

643 where $r(t)$ is the transcription rate (i.e., the mRNA production rate reported by MS2 fluorescence),
644 and $\gamma_R = 0.099 \text{ min}^{-1}$ (see [Table S1](#)). An example of a resulting prediction for the amount of mRNA
645 as a function of time is shown in [Figure S3C](#).

646 Next, we performed a parameter sweep for the translation rate α and, for each value of α , we
647 integrated $R(t)$ to predict the protein dynamics $P(t)$ using the following equation (see [Figure S3D](#)
648 for sample nuclear traces)

$$\frac{dP}{dt} = \alpha R(t) - \gamma_P P(t). \quad (\text{S18})$$

649 The translation rate that results in the best fit ([Figure S3D](#), red line) is recorded for each nu-
650 cleus. We then calculated α values for each embryo by averaging best-fitted α for each single cell
651 ([Figure S3E](#)). These values are averaged across $N = 129$ cells (embryo 1) and $N = 119$ cells (em-
652 bryo 2), respectively. Then we averaged the resulting value of α between two embryos, giving us
653 $\alpha = 0.082 \pm 0.004 \text{ protein AU (mRNA AU min)}^{-1}$ (see [Table S1](#)), which is used in our dynamical systems
654 model in the main text.

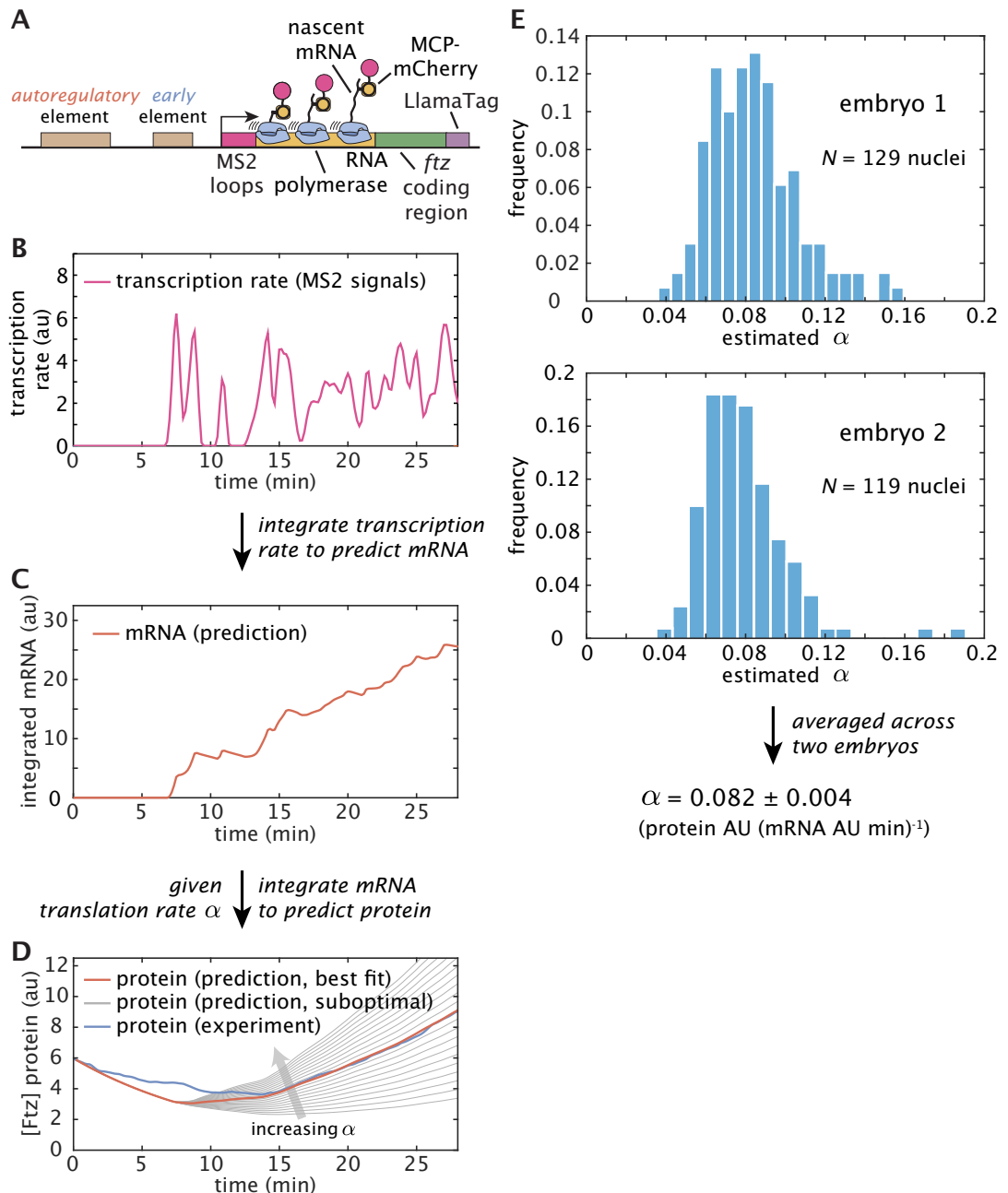


Figure S3. Procedure for estimating the translation rate α . (A) Ftz-MS2-LlamaTag transgenic construct used for estimating the translation rate. (B) Illustrative example of the raw MS2 traces that report on the instantaneous *ftz* transcription rate. MS2 traces are smoothed using a moving average of 1 min. (C) We integrate the MS2 traces to predict the mRNA dynamics in individual nuclei. (D) For a given value of the translation rate, we integrate the predicted mRNA dynamics to subsequently predict the Ftz protein dynamics in individual nuclei. The value of α that leads to the best agreement between prediction and experiment is found (red line). Suboptimal fits are shown as (gray lines). Ftz protein traces are smoothed using a moving average of 5 min. (E) Histogram distribution of best-fitted α values for individual cells within two embryos. Note that α values larger than 0.2 au are omitted for accuracy ($N = 2$ nuclei). We first calculated the average α for each individual embryo and then computed the average between these two embryos, resulting in $\alpha = 0.082 \pm 0.004$ protein AU (mRNA AU min)⁻¹, which is used in our dynamical systems model.

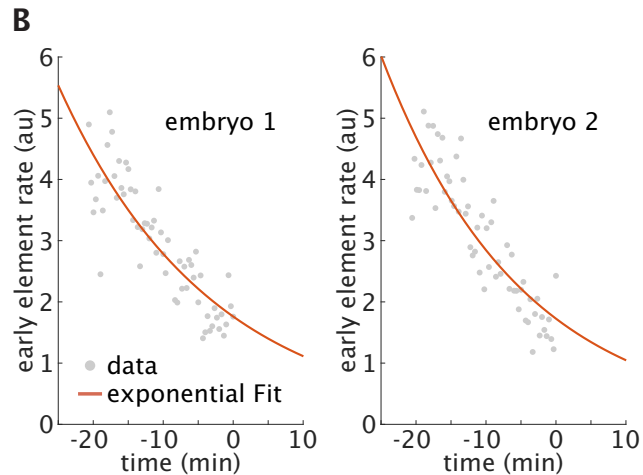
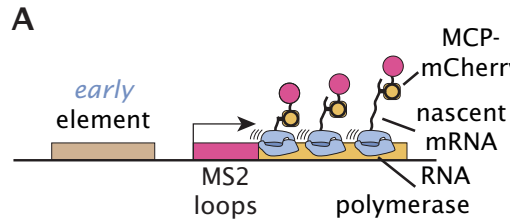


Figure S4. Inferring the decay rate of the early element transcriptional activity β . (A) Imaging transcriptional dynamics of the early element using the MS2 system. The construct is the same as the one described in **Figure 3A**. (B) Exponential fit from two embryos. Gray dots represent the averaged early element transcription rate at individual time points from a single embryo. Red line is the exponential fit that is used to estimate the early element decay rate β .

655 S2.3 Early element transcriptional activity decay rate β

656 We calculated the decay in the mRNA production rate of early element, described by the decay
 657 rate β , from fluorescence measurements of the early element MS2 reporter construct (**Figure S4A**).
 658 We performed an exponential fit to the average trajectory of each embryo (see **Figure S4B** for an
 659 example fit) and averaged the resulting decay rates to obtain the mean value $\beta = 0.048 \pm 0.0021$
 660 (see **Table S1**, $N = 2$ embryos) that we used in the dynamical systems model.

661 S2.4 Scaling factor c

662 We estimated c , the ratio of maximum production rate from the endogenous locus vs. the trans-
 663 gene, by approximating the solution to the dynamical system in **Eq. S4** between two time points
 664 for which we have empirical data. In particular, we began from the experimental observation that
 665 $\hat{f}(t, P)$ plateaus shortly before gastrulation for nuclei with total Ftz levels above about $P_{\infty}^{\text{thresh}} =$
 666 1.5×10^6 a.u. Therefore, for nuclei that satisfy $P_{\text{early}}(t) \geq P_{\infty}^{\text{thresh}}$ during this time (**Figure S5A**), we can
 667 approximate the nonlinear system for the autoregulatory element by the following *linear* system

$$\begin{cases} \frac{dR}{dt} = c f(P_{\infty}^{\text{thresh}}) - \gamma_R R(t) \\ \frac{dP}{dt} = \alpha R(t) - \gamma_P P(t) \end{cases}, \quad (\text{S19})$$

668 where $f(P_{\infty}^{thresh})$ is now a constant. This system of equations has an analytical solution given by

$$\begin{cases} R(t) = cR(0)e^{-\gamma_R t} + \frac{cf(P_{\infty}^{thresh})}{\gamma_R} (1 - e^{-\gamma_R t}) \\ P(t) = P(0)e^{-\gamma_P t} + \frac{\alpha}{\gamma_P - \gamma_R} \left(R(t) - R(0)e^{-\gamma_P t} - \frac{cf(P_{\infty}^{thresh})}{\gamma_P} (1 - e^{-\gamma_P t}) \right). \end{cases} \quad (\text{S20})$$

669 Rearranging these expressions gives

$$c = \frac{\gamma_P}{f(P_{\infty}^{thresh})(1 - e^{-\gamma_P t})} \left((R(t) - R(0)e^{-\gamma_P t}) - \frac{\gamma_P - \gamma_R}{\alpha} (P(t) - P(0)e^{-\gamma_P t}) \right). \quad (\text{S21})$$

670 Note that here $t = 0$ is assigned to the beginning of the time window over which the simulation is
671 performed.

672 We calculated the solution to [Eq. S21](#) for the individual boundary nuclei in the same embryos
673 as used to fit the gene regulatory function ([Figure 4D](#)). We restricted our estimations to the 3 min
674 before gastrulation based on personal observations that the prediction accuracy of the simulation
675 of this linearized system tended to fall after ~ 3 min. We derived the initial conditions $(R(0), P(0))$
676 from estimates of the late protein obtained by subtracting simulated early protein from the total
677 protein trace (where the autoregulatory element was assumed to begin contributing at -20 min
678 before gastrulation). We estimated c in a windowed approach whereby, for each nucleus, we simu-
679 lated only over one empirical sample interval (10 s) for all intervals from 3 min before gastrulation
680 ([Figure S5B](#)). We pooled all samples for individual time windows across all nuclei ([Figure S5C](#) and
681 D) and averaged them to give a final estimate of $c \approx 0.45 \pm 0.02$ across the 3 min before gastrulation
682 (where the error range is the standard error).

683 S3 Simulations

684 S3.1 Best predicted nuclei

685 In order to be assured of the accuracy of our conclusions concerning the dynamics of the com-
686 mitment process, in [Figure 7](#) we decided to restrict our analysis to sets of nuclei whose simulated
687 trajectories well matched the empirical traces. From our dataset, we identified such “best pre-
688 dicted” nuclei based on the cumulative error between a measured trajectory $\{(R_t, P_t)\}$ at discrete
689 time points t and a simulated trajectory $\{(\hat{R}_t, \hat{P}_t)\}$ at the same time points as

$$\epsilon = \sum_t \sqrt{(\hat{R}_t - R_t)^2 + (\hat{P}_t - P_t)^2}. \quad (\text{S22})$$

690 From a histogram of the errors ([Figure S6A](#)), which was roughly bimodal, we identified a threshold
691 of 7×10^7 to identify the 79 best predicted nuclei out of 118 nuclei total. Some sample traces from
692 these best predicted nuclei are shown in [Figure S6B](#) while traces for nuclei with high cumulative
693 error are shown in [Figure S6C](#).

694 We also calculated the cumulative error when simulations were conducted for a gradual in-
695 crease in autoregulatory responsiveness described by

$$\hat{f}(t, P) = (1 - e^{-\xi*(t-t_{on})}) f(P), \quad t > t_{on}, \quad (\text{S23})$$

696 where $f(P)$ is as defined in [Eq. S3](#) and $\xi = 0.14 \text{ min}^{-1}$ corresponds to a half-life of 5 min (from
697 the observation that the autoregulatory element transitions from unresponsive to fully responsive
698 over 10 min; see [Figure 4E](#)). The resulting sample traces are shown in [Figure S7B](#). Compared to
699 the case where we assume that the autoregulatory element becomes active instantaneously at t_{on}
700 ([Figure S6A](#)), there was a slight shift in the distribution toward lower error (88 best predicted with
701 the same cutoff as before in [Figure S6A](#)), but the binary classification accuracy at gastrulation was
702 the same. Therefore we opted to use $f(P)$ rather than $\hat{f}(t, P)$ for the main analysis.

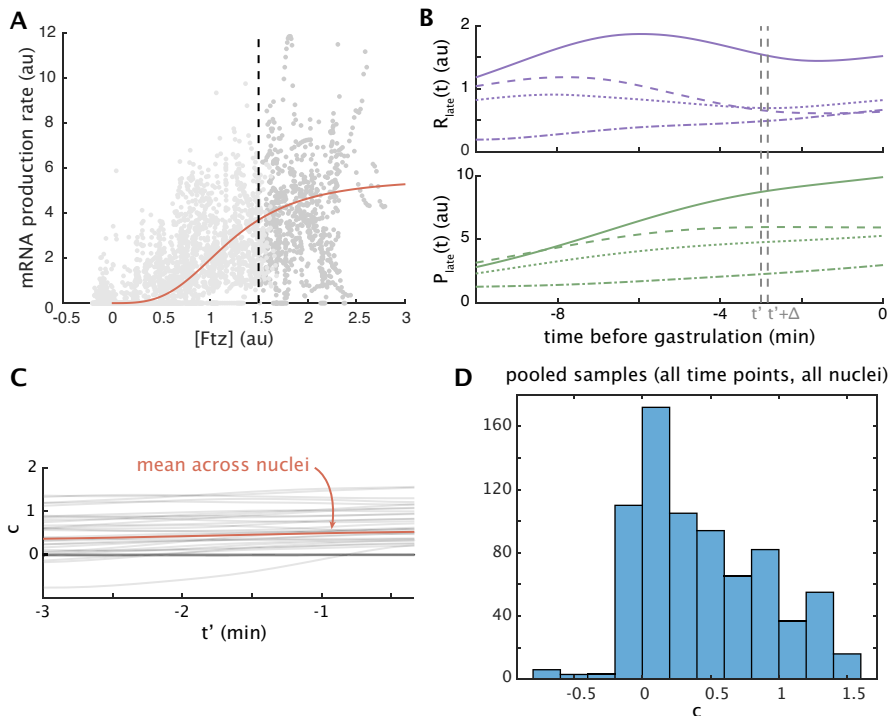


Figure S5. Procedure for estimating c , the ratio of the maximum mRNA production rate from the endogenous to the transgene. (A) We use a subset of samples for which the gene regulatory function is approximately saturated across the entire 3 min before gastrulation. Red, the gene regulatory function. Gray dots are individual time points from individual nuclei during the 3 min before gastrulation. Dark gray dots belong to nuclei for which $P_{total}(t) > P_{\infty, hresh}$ for all times between -3 and 0 min relative to gastrulation. Light gray dots correspond to nuclei that did not match this criterion. (B) Top, estimated late mRNA traces and bottom, estimated late protein traces for four sample nuclei drawn from the subset identified in (A). Gray dashed lines indicate one sample interval from t' to $t' + \Delta$ used to estimate c (see text). (C) Gray, estimates of c for each interval pictured in (B) and each nucleus identified in (A). Red, the mean at each time point across all nuclei. Note that most variation is between nuclei rather than across time points. (D) Histogram of c for all time intervals across all nuclei, mean 0.45, standard error 0.02.

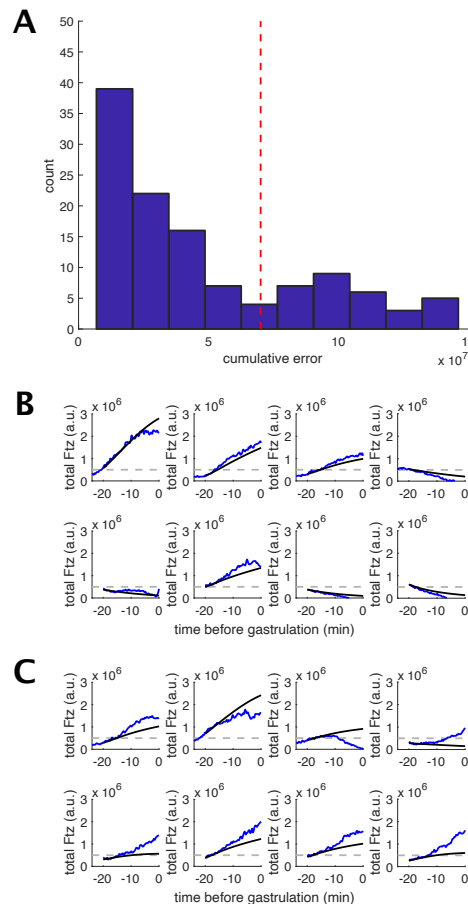


Figure S6. Classifying nuclei by the cumulative error in model prediction in a model of instantaneous autoregulation onset. (A) Histogram of cumulative errors for $N = 118$ nuclei. Simulations were conducted assuming that the autoregulatory element becomes instantaneously responsive, as in Eq. S3 and the main text. (B) Sample traces of best predicted nuclei. In each plot, the blue curve is the measured trace and the black line is the corresponding predicted trace. The dashed gray line is the threshold for classifying a nucleus as “on” at gastrulation. (C) As for (B), but for nuclei that did not qualify to be best predicted.

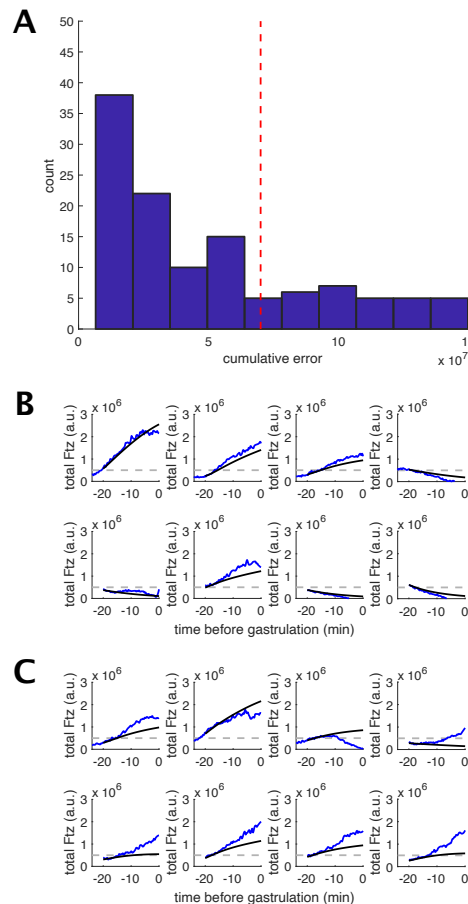


Figure S7. Classifying nuclei by the cumulative error in model prediction in a model of gradual autoregulation onset. (A) Histogram of cumulative errors for $N = 118$ nuclei. Simulations were conducted assuming a gradual increase in responsiveness of the autoregulatory element, following the dynamics in Eq. S23. (B) Sample traces of best predicted nuclei. In each plot, the blue curve is the measured trace and the black line is the corresponding predicted trace. The dashed gray line is the threshold for classifying a nucleus as “on” at gastrulation. (C) As for (B), but for nuclei that did not qualify to be best predicted.

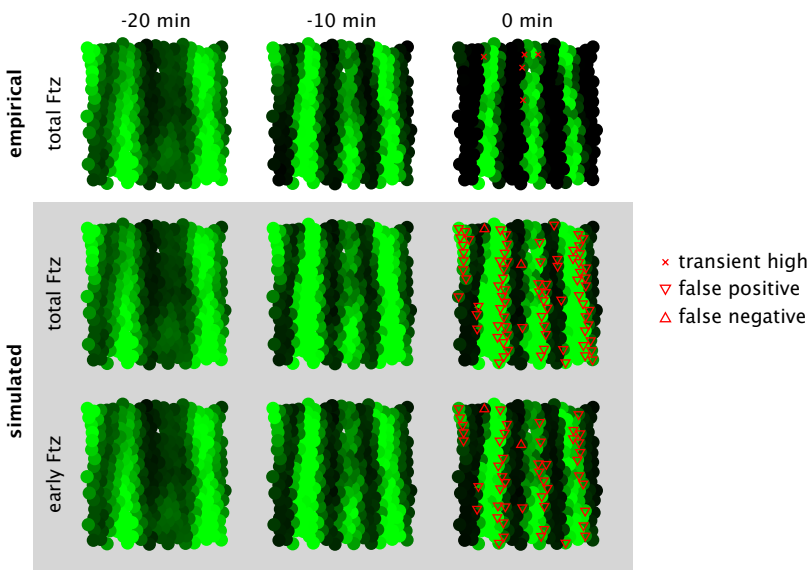


Figure S8. Whole-embryo simulation for the Ftz stripe pattern. Illustrative whole-embryo simulation for the same embryo as pictured in [Figure 6C](#). Pixel intensities are normalized to the steady-state high Ftz level.

703 **S3.2 Whole-embryo simulations**

704 We were curious about how accurately our model, which is based on measurements at the anterior
705 boundary of stripe 4, would predict Ftz state for all nuclei spanning stripes 3, 4 and 5 measured
706 during our experiments. Assuming all nuclei follow the same dynamics as given in [Eq. 5](#) and [Eq. S4](#),
707 we repeated the analysis from [Figure 5](#) to predict Ftz concentration at gastrulation. We achieved a
708 binary classification accuracy of (74.6%, or 763 of 1036 nuclei). Interestingly, this is worse than the
709 accuracy achieved from thresholding early protein alone (84.3%, or 873 of 1036 nuclei), which is
710 itself comparably accurate to the predictions for the anterior boundary of stripe 4 (with or without
711 the autoregulatory contribution). The bulk of classification errors for the whole-embryo sim-
712 ulations, whether from thresholding full simulations or thresholding early protein alone, were false
713 positives at the posterior boundaries of stripes, as in the example plotted in [Figure S8](#). This indi-
714 cates that something differs in the regulation of Ftz at the anterior boundaries of stripes as com-
715 pared to the posterior boundaries. For example, it has been noted that the posterior, but not the
716 anterior, boundaries of Ftz stripes are repressed by *sloppy paired* (*slp*) ([Clark, 2017](#)).

717 **S3.3 Delaying the onset of responsiveness of the autoregulatory element**

718 From a mathematical standpoint, we can treat a delay in t_{on} as a change in the starting time of
719 the simulation, which introduces a corresponding change to the initial conditions ($r(t_{on})$, $R_{early}(t_{on})$,
720 $P_{early}(t_{on})$) of the early module. In this way, the time at which the trajectory of the early module
721 ($r(t)$, $R_{early}(t)$, $P_{early}(t)$) crosses the switching separatrix is the latest time at which the autoregulatory
722 element can become responsive and still commit a cell to the appropriate (high) fate ([Figure S9](#)).
723 This follows from three conditions: (1) the early element is time invariant, (2) the early element is
724 independent of the autoregulatory module (the same is not true for the autoregulatory module,
725 which takes the output of the early module as its input), and (3) Ftz fate corresponds to the Ftz
726 concentration state at infinite time. (1) and (2) ensure that, even if we delay the autoregulatory ele-
727 ment, we can continue to use [Eq. 5](#) to simulate early protein by just changing the initial conditions,
728 while (3) ensures that the delayed start of the autoregulatory element will not change the location

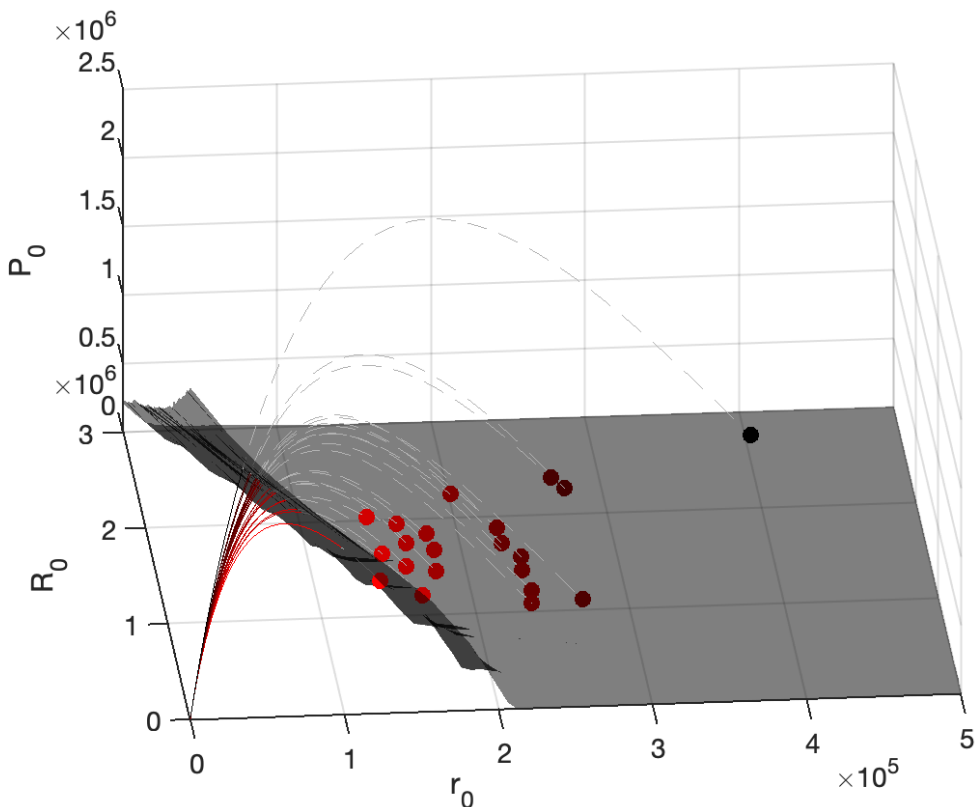


Figure S9. Sensitivity of Ftz fate to the autoregulatory onset time t_{on} . Dashed gray lines denote the trajectories $(r(t), R_{early}(t), P_{early}(t))$ corresponding to each nucleus. Trajectories begin at the colored points, each of which corresponds to the state of the early module in a high-fated nucleus ($N = 21$ same as analyzed in [Figure 7](#)) at time -20 min. Nuclei are colored based on the amount of time until the trajectory crosses the switching separatrix from [Figure 6B](#), with darker colors indicating longer times. As explained in the text, this crossing time corresponds to the longest acceptable delay in the onset of autoregulatory responsiveness without changing the fate of the cell. Intriguingly, the trajectories of early protein run parallel to the separatrix before converging to cross it in a restricted region of parameter space.

729 of the switching surface (which is relative to steady state, not to a transient state of the trajectory
730 at a fixed point in time).

731 In [Figure 7](#) we analyze the commitment window by varying t_{off} at the same time as t_{on} . In
732 [Figure S10](#) we report full results for simultaneous variation in t_{on} and t_{off} . The strictness with which
733 cell fate must be specified determines the variation in timing that can be tolerated. For example, if
734 the early element ceases production at or after gastrulation ($t_{off} > 0$), the autoregulatory element
735 can delay responsiveness until -15 min and still guide at least 75% of cells to the appropriate fate.
736 If the early element does not cease production until 20 min, then the autoregulatory element may
737 turn on just after -6 min and still direct 75% of cells to the correct fate. From these results, we see
738 that almost no cells commit to the high fate when $t_{on} > t_{off}$. For this reason, in the main text we
739 always set $t_{off} > t_{on}$.

740 **S3.4 Stochastic simulations**

741 Stochasticity in gene expression during embryonic development can compromise or improve sys-
742 tem function depending on the context ([Zhang et al., 2012; Papadopoulos et al., 2019](#)). We sought
743 to investigate whether stochasticity in gene expression (1) was sufficient to explain the prediction
744 error rates of our deterministic models, and (2) could drive stochastic switching at appreciable

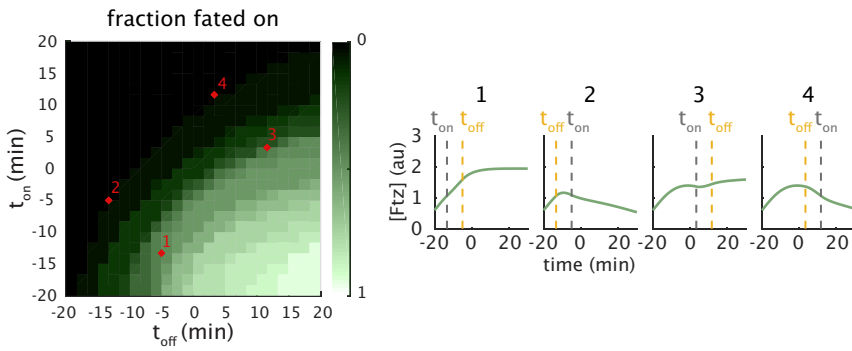


Figure S10. Dependence of Ftz fate adoption on the time that autoregulatory responsiveness begins and production rate from the early element shuts down. Left, heat map showing the fraction of cells predicted to adopt the high Ftz fate for different combinations of t_{on} and t_{off} . For this fraction to achieve 95% requires fairly strict coordination between the timing of modules, with neither event deviating more than about 7 min from $t_{on} = -20$ min or $t_{off} = 20$ min (on the order of the mRNA decay rate). Allowing for larger percentages of errors in fate determination significantly weakens constraints on regulatory timing, with a variation of up to 15 min in t_{off} or t_{on} still resulting in roughly 50% of cells adopting the appropriate high fate. Right, examples of simulated Ftz traces for a single nucleus with the timing conditions corresponding to the red marks on the heatmap.

745 rates. We examined these questions using stochastic differential equations (SDEs), assuming that
 746 the noise in our data arises solely from stochastic dynamics within the cells rather than from mea-
 747 surement noise. Generally, we expect this method to overestimate the error.

748 In a stochastic differential equation model, changes in the amount of late RNA dR_{late} and total
 749 protein dP_{total} over a time interval dt are given by

$$\begin{cases} dR_{late}(t) = (cf(P_{total}(t)) - \gamma_R R_{late}(t)) dt + \sigma_R(R_{late}(t))dW \\ dP_{total}(t) = (\alpha R_{tot}(t) - \gamma_P P_{total}(t)) dt + \sigma_P(P_{total}(t))dW, \end{cases} \quad (S24)$$

750 where dW is Gaussian with mean 0 and variance dt ([Gillespie, 2007](#)). The terms $\sigma_R(R_{late})$ and $\sigma_P(P_{late})$
 751 scale the variance of the noise from one time increment to the next.

752 For this analysis, we used our experimental setup featuring endogenous Ftz-LlamaTag driving
 753 an autoregulatory element transgene tagged with MS2 as introduced in [Figure 4](#). Because, over
 754 a small time interval where mRNA degradation is negligible, the MS2 signal reports on the rate of
 755 mRNA production, this signal gave us direct access to $dR_{late}(t_i)$ at discrete time points t_i . As a result,
 756 we can use this measure of $dR_{late}(t)$ to estimate for the late mRNA $R_{late}(t)$ by integrating the MS2
 757 signal following

$$R_{late}(t_i) = R_{late}(t_{i-1}) + dR_{late}(t_i)(t_i - t_{i-1}) \quad (S25)$$

758 under the assumption that $R_{late}(t_{on}) = 0$ (meaning that the autoregulatory element only becomes re-
 759 sponsive at time t_{on}). Since we also have direct measurements of $P_{total}(t)$, this allows us to rearrange
 760 [Eq. S24](#) so as to estimate the noise contribution $\sigma_R(R_{late}(t))dW$ from

$$\sigma_R(R_{late}(t))dW = dR_{late}(t) - (cf(P_{total}(t)) - \gamma_R R_{late}(t)) dt. \quad (S26)$$

761 If we further assume that $R_{early}(t)$ is noiseless and therefore given by the deterministic solution
 762 in [Eq. S9](#), we can estimate the total mRNA as $R_{total}(t) = R_{early}(t) + R_{late}(t)$. Then, since we have si-
 763 multaneous measurements of total Ftz protein P_{total} , we can also rearrange the lower equation in
 764 [Eq. S24](#) to estimate $\sigma_P(P_{total}(t))dW$ from

$$\sigma_P(P_{total}(t))dW = dP_{total}(t) - (\alpha R_{total}(t) - \gamma_P P_{total}(t)) dt. \quad (S27)$$

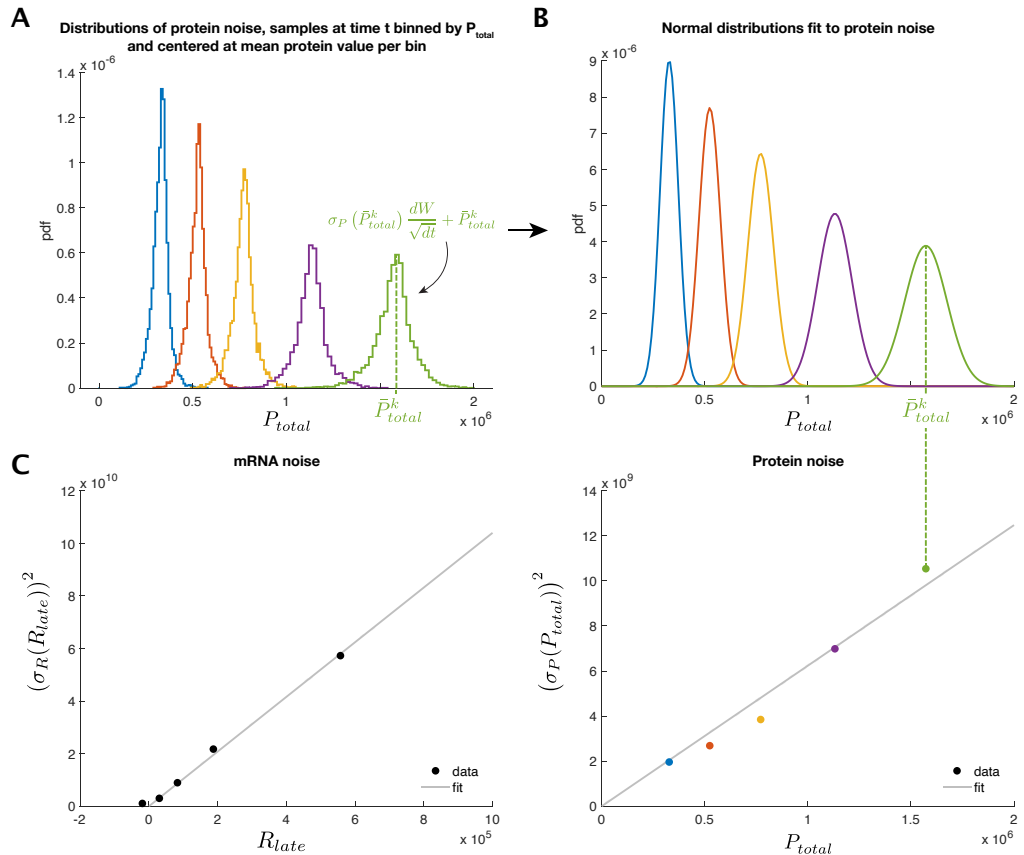


Figure S11. Procedure for estimating mRNA and protein expression noise. (A) We extract samples of the noise contribution for an individual sample point $\sigma_P(P_{total})dW$ following the method described in the text. We bin the samples by the corresponding P_{total} and calculate the mean protein level \bar{P}_{total}^k within each protein concentration bin k . We divide the samples by \sqrt{dt} to remove the variance contribution from the dW term in Eq. S24. We centered the samples from each bin at the corresponding \bar{P}_{total}^k to generate the pictured histograms. (B) A normal distribution is fitted to each bin in panel (A). (C) Right, we estimate $\sigma_P(P)$ by fitting a line to the relationship between \bar{P}_{total}^k and variance of the distribution fitted to the corresponding bin in (A) and (B). Left, the equivalent result for mRNA noise, which is calculated identically except that results are binned by $R_{late}(t)$ (not pictured).

765 We can perform the above analysis on individual measured traces to produce a large number
 766 of sample points of $\sigma_R(R_{late})dW$ and $\sigma_P(P_{total})dW$. With these data we will aim to estimate $\sigma_R(R)$
 767 and $\sigma_P(P)$. We assume the noise characteristics are time invariant, which allows us to pool all
 768 samples at all time points and bin them by the corresponding R_{late} or P_{total} . For example, for protein,
 769 we treat each protein concentration bin k as a population of samples of $\sigma_P(\bar{P}_{total}^k)dW$ where \bar{P}_{total}^k
 770 is the mean of the samples in bin k (Figure S11A). Since we assume dW is normally distributed
 771 with variance dt , we divide all sample values by \sqrt{dt} and fit a normal distribution to the resulting
 772 distribution within each protein concentration bin (Figure S11B). We found that the variances $\sigma_P(P)^2$
 773 are quite well approximated by a linear relation $\sigma_P(P)^2 = aP + b$ (Figure S11C, right). The mRNA
 774 variance was estimated similarly and also found to fit a linear relation (Figure S11C, left). Noise
 775 was estimated from all available trajectories, regardless of whether they were part of the stripe 4
 776 anterior boundary.

777 Having estimated the noise, we investigated whether stochasticity could explain the error rate
 778 in our predictions of Ftz expression state at gastrulation. We simulated $N_{sim} = 100$ experiments,

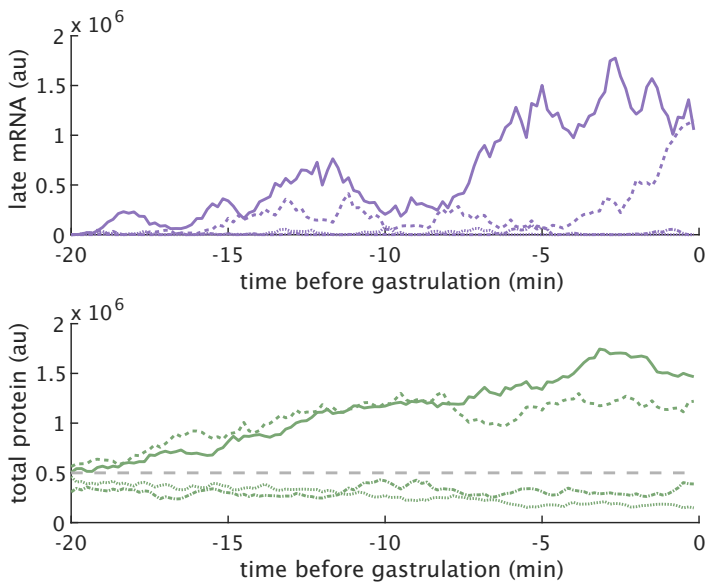


Figure S12. Sample traces for nuclei simulated with stochastic dynamics. Top, late mRNA and bottom, total protein traces simulated for individual nuclei obeying the stochastic dynamics in [Eq. S24](#). Gray dashed line in the bottom plot is the threshold to be classified as high Ftz at gastrulation.

each consisting of $N_{nuc} = 118$ nuclei evenly split between those deterministically predicted to be on and those deterministically predicted to be off. Specifically, we found the convex hull defined by the experimentally measured initial conditions for nuclei at the stripe 4 anterior boundary, and drew random initial conditions for the stochastically simulated nuclei from a uniform distribution within this hull. We assigned to each simulated experiment $\frac{N_{nuc}}{2}$ points below the blue surface in [Figure 5C](#) and $\frac{N_{nuc}}{2}$ above the surface without replacement (i.e., every nucleus in every simulated experiment has a unique set of initial conditions). Individual stochastic trajectories were generated using the Euler-Maruyama method, with the modification that protein and mRNA concentrations were forcibly lower bounded at 0 (i.e., random fluctuations that would bring concentrations to negative values were capped to instead bring the concentration to zero). Trajectories were simulated for 20 min until gastrulation and thresholded with the same value as for our deterministic simulations ([Figure S12](#)).

From our $N_{sim} = 100$ simulated experiments, we calculated a distribution of error rates given by

$$\frac{\text{total false positives} + \text{total false negatives}}{\text{total number nuclei}}, \quad (\text{S28})$$

where we compare the predicted outcomes from deterministic simulations to the “ground truth” of the stochastic simulations.

In [Figure S13](#) we plot the cumulative distribution of error rates for our simulations (black), broken down into false negatives (red) and false positives (green). The dashed vertical lines indicate the experimentally measured error rates with the same color code. Where the vertical lines intersect the corresponding cumulative distributions indicates the probability of measuring an error rate up to that rate. If the system is really described by the stochastic dynamics we have inferred, then the most likely error rates are those that intersect the curves where their slope is highest.

We found that the empirical error rate across 3 embryos was roughly twice that of the most likely error rates from our stochastic simulations corresponding to the middle of calculated cumulative distribution functions ([Figure S13](#), left), with the majority of errors being false negatives. We

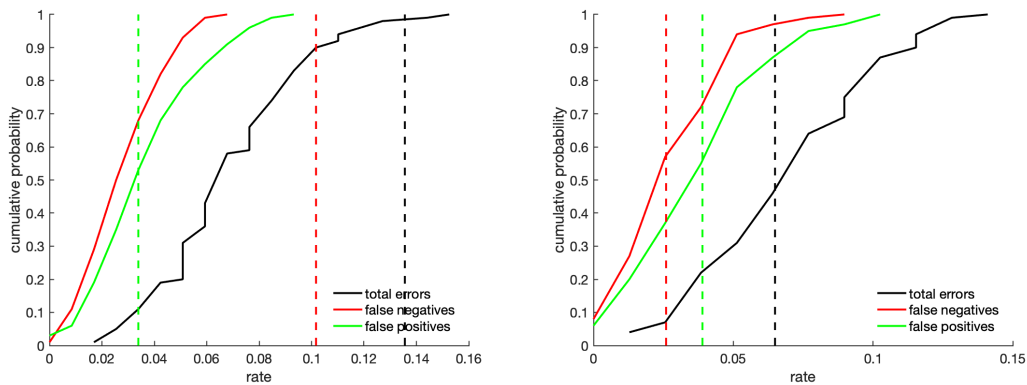


Figure S13. Error rates resulting from deterministic predictions made when gene expression is stochastic. Solid lines, cumulative distribution functions for error rates in the prediction of results for $N = 100$ simulated stochastic experiments (using the stochastic differential equation in Eq. S24), when using a deterministic simulation to make the predictions. For each simulation, we predicted the trajectories of N_{nuc} boundary nuclei evenly partitioned between starting states above and below the surface for classifying high or low Ftz at gastrulation (Figure 5). Dotted vertical lines correspond to empirical error rates for three embryos with $N_{nuc} = 118$ nuclei (left) across 3 embryos, or excluding one embryo that had a high number of deterministic false negatives (Section 2.3) for $N_{nuc} = 78$ nuclei (right) across 2 embryos.

803 knew from observation that one embryo had a large number of false negative predictions (Section 2.3,
804 and, interestingly, if we exclude this embryo from analysis, then the empirical error rate
805 aligns well with what the stochastic model predicts to be most likely (Figure S13, right). This result
806 suggests that many of our prediction errors can likely be attributed to stochastic fluctuations.

807 Having determined that the error of the model in predicting Ftz expression state at gastrulation
808 is comparable to the error expected when considering gene expression stochasticity, we next
809 turned to the question of whether gene expression stochasticity is expected to play a large role
810 in the long-term Ftz fate of cells in which the early element is no longer active. We ran $N = 100$
811 simulations beginning from the high steady state and calculated the distribution of first-passage
812 times to particular protein values (Figure S14, left) or to within some Euclidean distance of the op-
813 posite steady state (Figure S14, right). These measures give an approximation of the switching rate
814 depending upon how stringently one defines a threshold for switching.

815 Both trends indicate that switching from high to low occurs at a much faster rate than low to high,
816 with conservative rates of stochastic switching between the high and low Ftz fates of around
817 2 hr and between low and high fates of approximately 3 hr. For comparison of timescales, Ftz
818 stripes are no longer experimentally detected before the end of germband extension (Hafen et al.,
819 1984; Carroll, 1985), which occurs approximately 1.5 hours after gastrulation (da Silva and Vincent,
820 2007). Thus, we find no strong evidence that stochastic switching should contribute significantly to
821 Ftz stripe patterning.

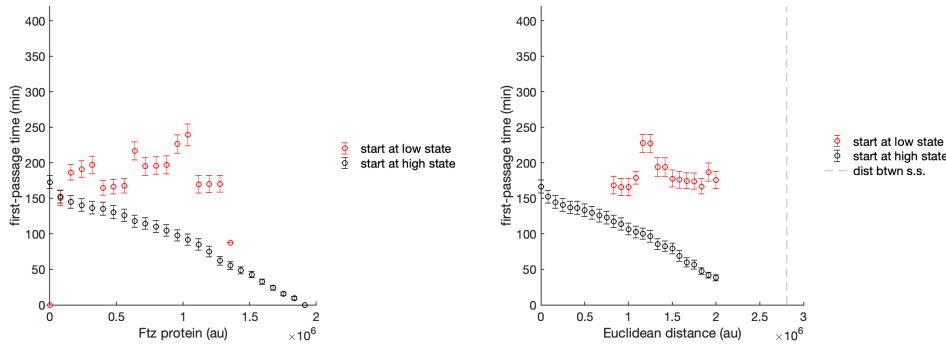


Figure S14. First-passage times suggest that the stochastic switching rate between Ftz fates at steady state occurs on a timescale of hours. Left, time to first passage of a stochastic trace starting from the high (black) or low (red) fate to a given protein value. Right, time to first passage of a stochastic trajectory with a given Euclidean distance from the opposite steady state. In both plots, red denotes simulations beginning in the low Ftz state and black denotes simulations beginning in the high Ftz state.

822 References

- 823 Alon, U. (2006). *An Introduction to Systems Biology*. Chapman and Hall/CRC.
- 824 Alon, U. (2007). Network motifs: Theory and experimental approaches. *Nature Reviews Genetics*, 8:450–461.
- 825 Angeli, D., Ferrell, J. E., and Sontag, E. D. (2004). Detection of multistability, bifurcations, and hysteresis in a large
826 class of biological positive-feedback systems. *Proceedings of the National Academy of Sciences*, 101(7):1822–
827 1827.
- 828 Bending, D., Martín, P. P., Paduraru, A., Ducker, C., Marzaganov, E., Laviron, M., Kitano, S., Miyachi, H., Crompton,
829 T., and Ono, M. (2018). A timer for analyzing temporally dynamic changes in transcription during differentiation
830 *in vivo*. *Journal of Cell Biology*, 217(8):2931–2950.
- 831 Blanchini, F. and Franco, E. (2014). Structural analysis of biological networks. In *A Systems Theoretic Approach to
832 Systems and Synthetic Biology I: Models and System Characterizations*, pages 47–71. Springer.
- 833 Bolouri, H. and Davidson, E. H. (2002). Modeling transcriptional regulatory networks. *BioEssays*, 24(12):1118–
834 1129.
- 835 Bothma, J. P., Garcia, H. G., Esposito, E., Schlissel, G., Gregor, T., and Levine, M. (2014). Dynamic regulation of
836 eve stripe 2 expression reveals transcriptional bursts in living *Drosophila* embryos. *Proceedings of the National
837 Academy of Sciences*, 111(29):10598–10603.
- 838 Bothma, J. P., Norstad, M. R., Alamos, S., and Garcia, H. G. (2018). LlamaTags: A versatile tool to image trans-
839 cription factor dynamics in live embryos. *Cell*, 173(7):1810–1822.
- 840 Bouchoucha, Y. X., Reingruber, J., Labalette, C., Wassef, M. A., Thierion, E., Desmarquet-Trin Dinh, C., Holcman,
841 D., Gilardi-Hebenstreit, P., and Charnay, P. (2013). Dissection of a Krox20 positive feedback loop driving cell
842 fate choices in hindbrain patterning. *Molecular Systems Biology*, 9:690.
- 843 Carroll, S. (1985). Localization of the *fushi tarazu* protein during *Drosophila* embryogenesis. *Cell*, 43(1):47–57.
- 844 Clark, E. (2017). Dynamic patterning by the *Drosophila* pair-rule network reconciles long-germ and short-germ
845 segmentation. *PLoS biology*, 15(9):e2002439.
- 846 Clark, E. and Akam, M. (2016). Odd-paired controls frequency doubling in *Drosophila* segmentation by altering
847 the pair-rule gene regulatory network. *eLife*, 5:e18215.
- 848 Clark, E., Battistara, M., and Benton, M. A. (2022). A timer gene network is spatially regulated by the terminal
849 system in the *Drosophila* embryo. *bioRxiv*.
- 850 Clark, E. and Peel, A. D. (2018). Evidence for the temporal regulation of insect segmentation by a conserved
851 sequence of transcription factors. *Development*, 145(10).

- 852 Corson, F. and Siggia, E. D. (2017). Gene-free methodology for cell fate dynamics during development. *eLife*,
853 6:e30743.
- 854 Cosentino, C. and Bates, D. (2011). *Feedback Control in Systems Biology*. CRC Press.
- 855 Cotterell, J. and Sharpe, J. (2010). An atlas of gene regulatory networks reveals multiple three-gene mechanisms
856 for interpreting morphogen gradients. *Molecular Systems Biology*, 6:425.
- 857 Crews, S. T. and Pearson, J. C. (2009). Transcriptional autoregulation in development. *Current Biology*,
858 19(6):R241–R246.
- 859 da Silva, S. M. and Vincent, J.-P. (2007). Oriented cell divisions in the extending germband of *Drosophila*. *Development*,
860 134(17):3049–3054.
- 861 Dalton, S. (2015). Linking the cell cycle to cell fate decisions. *Trends in Cell Biology*, 25(10):592–600.
- 862 Dearolf, C. R., Topol, J., and Parker, C. S. (1989). Transcriptional control of *Drosophila fushi tarazu* zebra stripe
863 expression. *Genes & development*, 3(3):384–398.
- 864 Del Vecchio, D., Densmore, D., El-Samad, H., Ingber, D., Khalil, A. S., Kosuri, Sri Lander, A. D., and Tang, C. (2016).
865 What have the principles of engineering taught us about biological systems? *Cell Systems*, 2:5–7.
- 866 Dubuis, J. O., Tkačík, G., Wieschaus, E. F., Gregor, T., and Bialek, W. (2013). Positional information, in bits.
867 *Proceedings of the National Academy of Sciences*, 110(41):16301–16308.
- 868 Edgar, B. A., Weir, M. P., Schubiger, G., and Kornberg, T. (1986). Repression and turnover pattern *fushi tarazu*
869 RNA in the early *Drosophila* embryo. *Cell*, 47(5):747–754.
- 870 Ferrell, J. E. (2002). Self-perpetuating states in signal transduction: positive feedback, double-negative feedback
871 and bistability. *Current Opinion in Cell Biology*, 14(2):140–148.
- 872 Furusawa, C. and Kaneko, K. (2012). A dynamical-systems view of stem cell biology. *Science*, 338(6104):215–217.
- 873 Garcia, H. G., Tikhonov, M., Lin, A., and Gregor, T. (2013). Quantitative imaging of transcription in living
874 *Drosophila* embryos links polymerase activity to patterning. *Current Biology*, 23(21):2140–2145.
- 875 Gillespie, D. T. (2007). Stochastic simulation of chemical kinetics. *Annual Review of Physical Chemistry*, 58(1):35–
876 55.
- 877 Goglia, A. G. and Toettcher, J. E. (2019). A bright future: Optogenetics to dissect the spatiotemporal control of
878 cell behavior. *Current Opinion in Chemical Biology*, 48:106–113.
- 879 Graham, P. L., Fischer, M. D., Giri, A., and Pick, L. (2021). The *fushi tarazu* zebra element is not required for
880 *Drosophila* viability or fertility. *G3*, 11(11).
- 881 Graham, T. G. W., Tabei, S. M. A., Dinner, A. R., and Rebay, I. (2010). Modeling bistable cell-fate choices in the
882 *Drosophila* eye: qualitative and quantitative perspectives. *Development*, 137(14):2265–2278.
- 883 Gratz, S. J., Rubinstein, C. D., Harrison, M. M., Wildonger, J., and O'Connor-Giles, K. M. (2015). CRISPR-Cas9
884 genome editing in *Drosophila*. *Current Protocols in Molecular Biology*, 111(1):1–31.
- 885 Gregor, T., Tank, D. W., Wieschaus, E. F., and Bialek, W. (2007). Probing the limits to positional information. *Cell*,
886 130(1):153–164.
- 887 Gutenkunst, R. N., Waterfall, J. J., Casey, F. P., Brown, K. S., Myers, C. R., and Sethna, J. P. (2007). Universally
888 sloppy parameter sensitivities in systems biology models. *PLoS Computational Biology*, 3(10):e189.
- 889 Hafen, E., Kuroiwa, A., and Gehring, W. J. (1984). Spatial distribution of transcripts from the segmentation gene
890 *fushi tarazu* during *Drosophila* embryonic development. *Cell*, 37:833–841.
- 891 Hartwell, L. H., Hopfield, J. J., Leibler, S., and Murray, A. W. (1999). From molecular to modular cell biology.
892 *Nature*, 402:C47–C52.
- 893 Hiromi, Y. and Gehring, W. J. (1987). Regulation and function of the *Drosophila* segmentation gene *fushi tarazu*.
894 *Cell*, 50(6):963–974.

- 895 Hiromi, Y., Kuroiwa, A., and Gehring, W. J. (1985). Control elements of the *Drosophila* segmentation gene *fushi tarazu*. *Cell*, 43(3):603–613.
- 896
- 897 Ingram, P. J., Stumpf, M. P. H., and Stark, J. (2006). Network motifs: structure does not determine function. *BMC Genomics*, 7:108.
- 898
- 899 Jaeger, J. and Monk, N. (2014). Bioattractors: Dynamical systems theory and the evolution of regulatory processes. *The Journal of Physiology*, 592(11):2267–2281.
- 900
- 901 Jaeger, J., Surkova, S., Blagov, M., Janssens, H., Kosman, D., Kozlov, K. N., Manu, Myasnikova, E., Vanario-Alonso, C. E., Samsonova, M., Sharp, D. H., and Reinitz, J. (2004). Dynamic control of positional information in the early *Drosophila* embryo. *Nature*, 430:368–371.
- 902
- 903
- 904 Johnson, H. E. and Toettcher, J. E. (2018). Illuminating developmental biology with cellular optogenetics. *Current Opinion in Biotechnology*, 52:42–48.
- 905
- 906 Khammash, M. (2016). An engineering viewpoint on biological robustness. *BMC Biology*, 14:22.
- 907
- 908 Kim, Y. J., Rhee, K., Liu, J., Jeammet, P., Turner, M., Small, S., and Garcia, H. G. (2021). Predictive modeling reveals that higher-order cooperativity drives transcriptional repression in a synthetic developmental enhancer. *bioRxiv*.
- 909
- 910 Kueh, H. Y., Champhekar, A., Nutt, S. L., Elowitz, M. B., and Rothenberg, E. V. (2013). Positive feedback between PU.1 and the cell cycle controls myeloid differentiation. *Science*, 341(6146):670–673.
- 911
- 912 Lai, K., Robertson, M. J., and Schaffer, D. V. (2004). The Sonic Hedgehog signaling system as a bistable genetic switch. *Biophysical Journal*, 86(5):2748–2757.
- 913
- 914 Lammers, N. C., Galstyan, V., Reimer, A., Medin, S. A., Wiggins, C. H., and Garcia, H. G. (2020). Multimodal transcriptional control of pattern formation in embryonic development. *Proceedings of the National Academy of Sciences of the United States of America*, 117(2):836–847.
- 915
- 916
- 917 Laslo, P., Spooner, C. J., Warmflash, A., Lancki, D. W., Lee, H.-J., Sciammas, R., Gantner, B. N., Dinner, A. R., and Singh, H. (2006). Multilineage transcriptional priming and determination of alternate hematopoietic cell fates. *Cell*, 126(4):755–766.
- 918
- 919
- 920 Lopes, F. J. P., Vieira, F. M. C., Holloway, D. M., Bisch, P. M., and Spirov, A. V. (2008). Spatial bistability generates hunchback expression sharpness in the *Drosophila* embryo. *PLoS Computational Biology*, 4(9):e1000184.
- 921
- 922 Lucas, T., Ferraro, T., Roelens, B., De Las Heras Chanes, J., Walczak, A. M., Coppey, M., and Dostatni, N. (2013). Live imaging of Bicoid-dependent transcription in *Drosophila* embryos. *Current Biology*, 23(21):2135–2139.
- 923
- 924 MacArthur, S., Li, X.-Y., Li, J., Brown, J. B., Chu, H. C., Zeng, L., Grondona, B. P., Hechmer, A., Simirenko, L., Keränen, S. V., Knowles, D. W., Stapleton, M., Bickel, P., Biggin, M. D., and Eisen, M. B. (2009). Developmental roles of 21 *Drosophila* transcription factors are determined by quantitative differences in binding to an overlapping set of thousands of genomic regions. *Genome Biology*, 10(7):R80.
- 925
- 926
- 927
- 928 Manu, Surkova, S., Spirov, A. V., Gursky, V. V., Janssens, H., Kim, A.-R., Radulescu, O., Vanario-Alonso, C. E., Sharp, D. H., Samsonova, M., and Reinitz, J. (2009). Canalization of gene expression in the *Drosophila* blastoderm by gap gene cross regulation. *PLoS Biology*, 7(3):e1000049.
- 929
- 930
- 931 McNamara, H. M., Ramm, B., and Toettcher, J. E. (2022). Synthetic developmental biology: New tools to deconstruct and rebuild developmental systems. *Seminars in Cell & Developmental Biology*.
- 932
- 933 McNeely, K. C. and Dwyer, N. D. (2021). Cytokinetic abscission regulation in neural stem cells and tissue development. *Current Stem Cell Reports*, 7(4):161–173.
- 934
- 935 Nüsslein-Volhard, C. and Wieschaus, E. (1980). Mutations affecting segment number and polarity in *Drosophila*. *Nature*, 287(5785):795–801.
- 936
- 937 Papadopoulos, D. K., Skouloudaki, K., Engström, Y., Terenius, L., Rigler, R., Zechner, C., Vukojević, V., and Tomancak, P. (2019). Control of Hox transcription factor concentration and cell-to-cell variability by an auto-regulatory switch. *Development*.
- 938
- 939

- 940 Papatsenko, D. and Levine, M. (2011). The *Drosophila* gap gene network is composed of two parallel toggle
941 switches. *PLoS ONE*, 6(7):e21145.
- 942 Peter, I. S. and Davidson, E. H. (2015). *Genomic control process: development and evolution*. Academic Press.
- 943 Petkova, M. D., Tkačik, G., Bialek, W., Wieschaus, E. F., and Gregor, T. (2019). Optimal decoding of cellular
944 identities in a genetic network. *Cell*, 176(4):844–855.e15.
- 945 Pezzotta, A. and Briscoe, J. (2022). Optimal control of gene regulatory networks for morphogen-driven tissue
946 patterning. *bioRxiv*.
- 947 Pick, L., Schier, A., Affolter, M., Schmidt-Glenewinkel, T., and Gehring, W. J. (1990). Analysis of the *ftz* upstream element:
948 Germ layer-specific enhancers are independently autoregulated. *Genes and Development*, 4(7):1224–
949 1239.
- 950 Reimer, A., Alamos, S., Westrum, C., Turner, M. A., Talledo, P., Zhao, J., and Garcia, H. G. (2021). Minimal synthetic
951 enhancers reveal control of the probability of transcriptional engagement and its timing by a morphogen
952 gradient. *bioRxiv*.
- 953 Sáez, M., Blassberg, R., Camacho-Aguilar, E., Siggia, E. D., Rand, D. A., and Briscoe, J. (2022). Statistically derived
954 geometrical landscapes capture principles of decision-making dynamics during cell fate transitions. *Cell
955 Systems*, 13(1):12–28.
- 956 Schier, A. F. and Gehring, W. J. (1992). Direct homeodomain–DNA interaction in the autoregulation of the *fushi
tarazu* gene. *Nature*, 356(6372):804–807.
- 957 Schier, A. F. and Gehring, W. J. (1993). Analysis of a *fushi tarazu* autoregulatory element: Multiple sequence
958 elements contribute to enhancer activity. *EMBO Journal*, 12(3):1111–1119.
- 959 Schroeder, M. D., Greer, C., and Gaul, U. (2011). How to make stripes: Deciphering the transition from non-
960 periodic to periodic patterns in *Drosophila* segmentation. *Development*, 138(14):3067–3078.
- 961 Soldatov, R., Kaucka, M., Kastriti, M. E., Petersen, J., Chontorotzea, T., Englmaier, L., Akkuratova, N., Yang, Y.,
962 Häring, M., Dyachuk, V., Bock, C., Farlik, M., Piacentino, M. L., Boismoreau, F., Hilscher, M. M., Yokota, C.,
963 Qian, X., Nilsson, M., Bronner, M. E., Croci, L., Hsiao, W.-Y., Guertin, D. A., Brunet, J.-F., Consalez, G. G., Ernfors,
964 P., Fried, K., Kharchenko, P. V., and Adameyko, I. (2019). Spatiotemporal structure of cell fate decisions in
965 murine neural crest. *Science*, 364(6444).
- 966 Soluri, I. V., Zumerling, L. M., Payan Parra, O. A., Clark, E. G., and Blythe, S. A. (2020). Zygotic pioneer factor
967 activity of Odd-paired/Zic is necessary for late function of the *Drosophila* segmentation network. *eLife*, 9.
- 968 Sootla, A., Oyarzún, D., Angeli, D., and Stan, G.-B. (2016). Shaping pulses to control bistable systems: Analysis,
969 computation and counterexamples. *Automatica*, 63:254–264.
- 970 Sprinzak, D., Lakhanpal, A., LeBon, L., Santat, L. A., Fontes, M. E., Anderson, G. A., Garcia-Ojalvo, J., and Elowitz,
971 M. B. (2010). *Cis*-interactions between Notch and Delta generate mutually exclusive signalling states. *Nature*,
972 465:86–90.
- 973 Srinivasan, S., Hu, J. S., Currle, D. S., Fung, E. S., Hayes, W. B., Lander, A. D., and Monuki, E. S. (2014). A BMP-FGF
974 morphogen toggle switch drives the ultrasensitive expression of multiple genes in the developing forebrain.
975 *PLoS Computational Biology*, 10(2):e1003463.
- 976 Tkačik, G. and Gregor, T. (2021). The many bits of positional information. *Development*, 148(2):dev176065.
- 977 Verd, B., Crombach, A., and Jaeger, J. (2017). Dynamic maternal gradients control timing and shift-rates for
978 *Drosophila* gap gene expression. *PLoS Computational Biology*, 13:e1005285.
- 979 Verd, B., Monk, N. A., and Jaeger, J. (2019). Modularity, criticality, and evolvability of a developmental gene
980 regulatory network. *eLife*, 8:e42832.
- 981 Villaverde, A. F., Henriques, D., Smallbone, K., Bongard, S., Schmid, J., Cicin-Sain, D., Crombach, A., Saez-
982 Rodriguez, J., Mauch, K., Balsa-Canto, E., Mendes, P., Jaeger, J., and Banga, J. R. (2015). BioPreDyn-bench:
983 a suite of benchmark problems for dynamic modelling in systems biology. *BMC Systems Biology*, 9(1).

- 985 von Dassow, G., Meir, E., Munro, E. M., and Odell, G. M. (2000). The segment polarity network is a robust
986 developmental module. *Nature*, 406(6792):188–192.
- 987 Waddington, C. (1957). *The Strategy of the Genes*. Routledge.
- 988 Wakimoto, B. T., Turner, F. R., and Kaufman, T. C. (1984). Defects in embryogenesis in mutants associated with
989 the antennapedia gene complex of *Drosophila melanogaster*. *Developmental biology*, 102(1):147–172.
- 990 Wang, J., Zhang, K., Xu, L., and Wang, E. (2011). Quantifying the Waddington landscape and biological paths for
991 development and differentiation. *Proceedings of the National Academy of Sciences*, 108(20):8257–8262.
- 992 Weiner, A. J., Scott, M. P., and Kaufman, T. C. (1984). A molecular analysis of *fushi tarazu*, a gene in *Drosophila*
993 *melanogaster* that encodes a product affecting embryonic segment number and cell fate. *Cell*, 37:843–851.
- 994 Wieland, F.-G., Hauber, A. L., Rosenblatt, M., Tönsing, C., and Timmer, J. (2021). On structural and practical
995 identifiability. *Current Opinion in Systems Biology*, 25:60–69.
- 996 Xiong, W. and Ferrell, J. E. (2007). A positive-feedback-based bistable ‘memory module’ that governs a cell fate
997 decision. *Nature*, 448(7157):1076–1076.
- 998 Zernicka-Goetz, M., Morris, S. A., and Bruce, A. W. (2009). Making a firm decision: multifaceted regulation of
999 cell fate in the early mouse embryo. *Nature Reviews Genetics*, 10(7):467–477.
- 1000 Zhang, L., Radtke, K., Zheng, L., Cai, A. Q., Schilling, T. F., and Nie, Q. (2012). Noise drives sharpening of gene
1001 expression boundaries in the zebrafish hindbrain. *Molecular Systems Biology*, 8(1):613.